

# Distributed assimilation of satellite-based snow extent for improving simulated streamflow in mountainous, dense forests: An example over the DMIP2 western basins

Soni Yatheendradas,<sup>1,2</sup> Christa D. Peters Lidard,<sup>2</sup> Victor Koren,<sup>3</sup> Brian A. Cosgrove,<sup>3</sup> Luis G. G. De Goncalves,<sup>4</sup> Michael Smith,<sup>3</sup> Jim Geiger,<sup>5</sup> Zhengtao Cui,<sup>3</sup> Jordan Borak,<sup>1,2</sup> Sujay V. Kumar,<sup>2,6</sup> David L. Toll,<sup>2</sup> George Riggs,<sup>7,8</sup> and Naoki Mizukami<sup>3,9</sup>

Received 30 August 2011; revised 24 July 2012; accepted 7 August 2012; published 29 September 2012.

[1] Snow cover area affects snowmelt, soil moisture, evapotranspiration, and ultimately streamflow. For the Distributed Model Intercomparison Project – Phase 2 Western basins, we assimilate satellite-based fractional snow cover area (fSCA) from the Moderate Resolution Imaging Spectroradiometer, or MODIS, into the National Weather Service (NWS) SNOW-17 model. This model is coupled with the NWS Sacramento Heat Transfer (SAC-HT) model inside the National Aeronautics and Space Administration's (NASA) Land Information System. SNOW-17 computes fSCA from snow water equivalent (SWE) values using an areal depletion curve. Using a direct insertion, we assimilate fSCAs in two fully distributed ways: (1) we update the curve by attempting SWE preservation, and (2) we reconstruct SWEs using the curve. The preceding are refinements of an existing simple, conceptually guided NWS algorithm. Satellite fSCA over dense forests inadequately accounts for below-canopy snow, degrading simulated streamflow upon assimilation during snowmelt. Accordingly, we implement a below-canopy allowance during assimilation. This simplistic allowance and direct insertion are found to be inadequate for improving calibrated results, still degrading them as mentioned above. However, for streamflow volume for the uncalibrated runs, we obtain: (1) substantial to major improvements (64–81%) as a percentage of the control run residuals (or distance from observations), and (2) minor improvements (16–22%) as a percentage of observed values. We highlight the need for detailed representations of canopy-snow optical radiative transfer processes in mountainous, dense forest regions if assimilation-based improvements are to be seen in calibrated runs over these areas.

**Citation:** Yatheendradas, S., et al. (2012), Distributed assimilation of satellite-based snow extent for improving simulated streamflow in mountainous, dense forests: An example over the DMIP2 western basins, *Water Resour. Res.*, 48, W09557, doi:10.1029/2011WR011347.

<sup>1</sup>Earth System Science Interdisciplinary Center, College Park, Maryland, USA.

<sup>2</sup>Hydrological Sciences Laboratory, NASA Goddard Space Flight Center, Greenbelt, Maryland, USA.

<sup>3</sup>Office of Hydrologic Development, Hydrology Laboratory, National Weather Service, Silver Spring, Maryland, USA.

<sup>4</sup>Group on Data Assimilation Development, DMD/CPTEC/INPE, Cachoeira Paulista, Brazil.

<sup>5</sup>NASA Goddard Space Flight Center, Greenbelt, Maryland, USA.

<sup>6</sup>Science Applications International Corporation, Beltsville, Maryland, USA.

<sup>7</sup>Science Systems and Applications Inc., Lanham, Maryland, USA.

<sup>8</sup>Cryospheric Sciences Branch, NASA Goddard Space Flight Center, Greenbelt, Maryland, USA.

<sup>9</sup>National Center for Atmospheric Research, Boulder, Colorado, USA.

Corresponding author: S. Yatheendradas, Hydrological Sciences Laboratory, NASA Goddard Space Flight Center, Greenbelt, MD 20771, USA. (soni.yatheendradas@nasa.gov)

Published in 2012 by the American Geophysical Union.

## 1. Introduction

[2] Snow stores and releases water at different time scales, providing a significant portion of runoff and the human water supply, both globally (e.g., one-sixth of the population: *Bartlett et al.* [2005]) and particularly over snowmelt-dominated regions (e.g., half in the Western US: *Serreze et al.* [2001]). Snowpack-caused runoff delay has major relevance for hydrologic models simulating downstream surface and groundwater availability for coupling with water use models (e.g., *Schmid and Hanson* [2009] coupling with irrigated agriculture model for Western US Sierra Nevada).

[3] In many current hydrologic and land surface models, mountain region simulations reflect snow parameterization limitations related to inadequate model representation of forcing, topography, net radiation, fractional snow cover and interactions with mainly forest vegetation, among other factors [e.g., *Nijssen et al.*, 2003]. However, accurate spatial distribution of snow properties in these regions, including fractional snow covered area or extent (fSCA) is considered important for adequately predicting snowmelt, soil moisture,

evapotranspiration, and ultimately streamflow. Besides the commonly studied snow depth, fSCA also directly influences snow energy and mass balances to provide melt and streamflow [Blöschl, 1991]. The fSCA also strongly affects the land surface energy balance in weather and climate models through high snow albedo.

[4] This study focuses on improving modeled streamflow by assimilating satellite-based fSCA for the challenging case of mountainous, dense forests. Past studies in such basins have struggled to demonstrate improvements in late melt-season streamflow simulations through late melt-season fSCA assimilation. Example workarounds accordingly employed are switching off the assimilation during the late melt season to avoid degrading simulations, and using assimilation-based forecasts starting earlier in the melt season. With this in mind, we attempt to reject the null hypothesis that the state assimilation of fSCA during the late melt season does not improve late melt-season streamflow simulations in a prediction sense. Section 2 provides a literature review of the effect of densely forested canopy on remotely sensed snow extent. This is followed by a review of the influence of fSCA assimilation on modeled streamflow in section 3. Next, sections 4 and 5 detail the study basins and data, and the model and assimilation methodology used. Finally, sections 6 and 7 cover the analysis of results, discussions and recommendations for future work.

## 2. Snow Extent Data and the Densely Forested Canopy Effect

[5] Satellite data have unmatched spatial and temporal coverage, providing fSCA estimates which could potentially improve hydrologic predictions. However, such fSCA maps can feature significant topography-caused noise over mountains [Nagler et al., 2008]. Dense canopy coverage can have an even greater effect: existing simple representations of canopy radiative transfer in most remotely sensed snow product algorithms are inadequate for use over forests, wherein “remain one of the largest sources of uncertainty in the remote sensing of snow” for both electro-optical and microwave sensors [e.g., Essery et al., 2009; Foster et al., 1991; Hall et al., 1998; Simic et al., 2004; Vikhamar and Solberg, 2002]. Also, especially underneath the canopy, blockage from trees makes forest snow mapping more difficult at large off-nadir sensor view angles (e.g., for the Moderate Resolution Imaging Spectroradiometer or MODIS sensor; <http://modis.gsfc.nasa.gov/>) [e.g., Hall et al., 1998, 2001; Liu et al., 2008; Dozier et al., 2008].

[6] Remotely sensed snow mapping uncertainty depends mainly on forest canopy type and density, e.g., microwave estimates degrade for densities above 60–70% [Cline et al., 2004; Pulliainen et al., 2001], and electro-optical instruments like MODIS underestimate snow for closed-canopy evergreen forests when compared against open-canopy areas [Simic et al., 2004]. Limited information gleaned from viewable canopy gaps is insufficient to establish the below-canopy snow extent [e.g., Essery et al., 2009]. Some factors causing differences between snow extents on and below the canopy include: canopies shading underlying snow from both direct and diffuse solar radiation [e.g., Pomeroy and Dion, 1996], and the nature of net radiation

in dense canopies where sometimes increased longwave radiation [Pomeroy and Granger, 1997] and even convective terms [Sicart et al., 2004] potentially outweigh the effects of decreased shortwave radiation.

[7] Field studies have investigated the relative snow amounts, extents and durations present in open areas, forest canopy gaps, above the canopy, and below the canopy (see citations in the modeling study Rutter et al. [2009] and Varhola et al. [2010]). While adjusting the remotely sensed snow depth using field measurements of forest cover has been attempted, e.g., for passive microwave observations [e.g., Armstrong and Brodzik, 2001; Clifford, 2010], the corresponding fSCA adjustment has received limited attention other than the simple assumption that the fSCA value in the forested portion of the pixel is same as that in the entire pixel [Molotch and Margulis, 2008]. Studies attempting better field-based fSCA adjustment include those by Liu et al. [2008] investigating the dependence of the sensor-viewable snow extent on the view angle, and Rice et al. [2010] conducting intensive in-situ gridded measurements of snow presence to adjust biases in the MODIS-derived MODSCAG product [Painter et al., 2009] for hydrologic modeling over the Sierra Nevada.

[8] Note that snow-vegetation radiative interactions can also complicate fSCA mapping indirectly based on snow-free vegetation properties and extents. For example, Robin et al. [2007] found vegetation index retrievals complicated by the presence of coniferous forest snow.

[9] Efforts to improve snow parameterizations have traditionally been associated with open areas, and hence are mostly inadequate for forested areas [Essery et al., 2009] where the above mentioned knowledge gap relating overall snow extents to those in viewable canopy gaps remains. One option to obtain or properly utilize the remotely sensed fSCA is to use detailed 3-dimensional canopy radiative transfer [Pinty et al., 2004] techniques, such as a geometric optical-radiative transfer component using view angles, canopy profile and density, etc. to calculate variables like the viewable gap fraction [Liu et al., 2008]. This can be applied either in the remotely sensed product algorithm or the corresponding postprocessor, or in the hydrology model itself as in Hardy et al. [1997].

## 3. Existing Studies of the Influence of fSCA Assimilation on Simulated Streamflow

[10] Most existing fSCA assimilation studies [e.g., Liston et al., 1999; Rodell and Houser, 2004; Andreadis and Lettenmaier, 2006; Molotch and Margulis, 2008; Su et al., 2008; De Lannoy et al., 2012] focused on improving modeled snow water equivalent (SWE), with a minority focusing on improving streamflow. Nonassimilation studies focused on improving streamflow include those where fSCA was used directly as an input (forcing) [e.g., Li and Williams, 2008], or for model calibration [e.g., Udnaes et al., 2007; Parajka and Blöschl, 2008; Finger et al., 2011]. Below, we only discuss studies of the effect of fSCA assimilation on the modeled runoff/streamflow.

[11] Studies assimilating fSCA to improve streamflow had varying results: (1) Johansson et al. [2003] found ambiguous results when the model states are reset to those of the closest date where modeled fSCA equals the

observation; (2) *Huttunen et al.* [2005] obtained mixed results on a boreal drainage basin; (3) *Dressler et al.* [2006] obtained reduced and increased streamflow simulation performance, respectively, for relatively complex and relatively homogeneous terrains in snow-dominated basins, with the performance of the former catching up with that of its nonassimilation counterpart when the assimilation was limited to the accumulation season; (4) *Clark et al.* [2006] found only minor improvements near the end of snowmelt season; (5) *McGuire et al.* [2006] showed the best improvements in forecasts made earliest in the melt season; (6) *Udnaes et al.* [2007] found that only some updates improved runoff, and most frequently at large SCA values; (7) *Zaitchik and Rodell* [2009] compared runoff as an ‘unconditioned’ sensitivity exercise (i.e., no comparison against actual observations) to show an increase and improvement in simulated snow volume, though their Figure 4 shows difficulty in simulating late-season SWE over the West Coast; (8) *Roy et al.* [2010] observed varying improvement in the streamflow Nash-Sutcliffe coefficient and the Root Mean Square Error (RMSE) using MODIS and NOAA IMS (National Oceanic and Atmospheric Administration Ice Mapping System) snow area data; (9) *Tang and Lettenmaier* [2010] found streamflow simulation errors were not necessarily reduced, with 2-week lead-time forecasts during snow ablation improving but not seasonal forecasts; (10) *Thirel et al.* [2011] found that discharge improved using the particle filter assimilation method but deteriorated with the ensemble Kalman filter; and (11) *Arsenault* [2011] also performed an unconditioned sensitivity exercise at SNOTEL-coincident locations and demonstrated a reduction in snow mass and hence runoff during melt. Below, we highlight the similarities and differences between these studies and this paper.

[12] Our study basins’ physiography includes the double complexity of being mountainous and densely forested, with earlier studies mostly featuring one of these factors. The only successful study incorporating both seems to be by *Roy et al.* [2010] conducted over mostly forested basins (the Du Nord watershed is 96.2% forest-covered with 47.7% evergreen, and the Aux Écorces basin is 83.5% forested with 12.3% evergreen). Somewhat puzzling is their improvement in streamflow even though their Figure 3 shows MODIS SCA decreasing relatively early to 0. Their methodology inserts a large 4 cm snow value into a snow-free model grid box when MODIS indicates snow but the model does not (see section 5.2: our study insertion is ~5 mm). The authors explain that this value possibly compensates for factors like the underestimation of winter precipitation; however, streamflow in their control simulation (which lacks such a compensation) does not follow the early decrease of the MODIS SCA. We speculate that a significant reason for their streamflow improvement is their large 4 cm snow insertion, since, per *Simic et al.* [2004]: (1) their Figure 8 shows Canadian evergreen and deciduous forests having a comparatively higher percentage of snow commission error than of omission, and (2) the 1 cm threshold is most representative of areal snow cover within the pixel.

[13] Regarding the transition to bare ground, *Clark et al.* [2006], *Roy et al.* [2010] and *Udnaes et al.* [2007] (some basins) with differing streamflow improvement results faced the problems of: (1) a substantial proportion of spring streamflow occurring before any bare ground is

exposed, and (2) the transition from 100% snow-covered to snow-free conditions occurring fairly quickly. The rapid snow melt is evident in the *Zaitchik and Rodell* [2009] and *Thirel et al.* [2011] studies.

[14] While other studies used fractional-valued spatial aggregates of binary snow/no-snow data [e.g., *Roy et al.*, 2010; *Thirel et al.*, 2011], our study assimilates fSCA at its base resolution. This is conceptually similar to *Dressler et al.* [2006], *Udnaes et al.* [2007] and *Arsenault* [2011], and to *Clark et al.* [2006] who used synthetic fSCA. Also, our snow model areal depletion curve (ADC) considers more depletion behavior characteristics than the simple ADC typically used, incorporating: (1) interannual consistency in the spatial pattern of relative snow amounts through a simple uniform scaling of the ADC shape across years, and (2) a temporary deviation of fSCA off the curve along a “new snow” line to 100% and back when a minimum new snowfall occurs on a partially bare area. While the ‘new snow’ line concept rarely exists in other studies (e.g., *Huttunen et al.* [2005]), the ADC shape preservation and scaling between years is present in the *Johansson et al.* [2003], *Dressler et al.* [2006], *McGuire et al.* [2006], and *Tang and Lettenmaier* [2010] studies (see *Andreadis and Lettenmaier* [2006] for details on the latter two). Typically, other models, e.g., the Noah LSM [*Chen et al.*, 1996; *Ek et al.*, 2003] investigated by *Zaitchik and Rodell* [2009], have fixed ADCs that depend only on land cover (i.e., the depletion curve SWE at the maximum fSCA is a fixed maximum and does not reflect the variation in these maximum SWEs among different accumulation periods).

[15] Previous studies have also used multiple fSCA assimilation methods including: (1) resetting model states to those of the closest date where the modeled fSCA equals the observation [*Johansson et al.*, 2003], (2) sequentially correcting the simulation by changing inputs such as temperature, precipitation and potential evaporation so that the observed SCA and other measured states agree with simulations [*Huttunen et al.*, 2005], and (3) multiplying a snow depth with the snow extent to get effective SWE for a pixel as in *Dressler et al.* [2006]. Regardless, the assimilation approach is typically either threshold-based or ADC-based using the fSCA versus SWE-based ADC. While our (and most other) studies follow the latter approach, some studies utilized rule-based updating where the snow presence decision is based on an fSCA threshold at the model’s resolution, e.g., *McGuire et al.* [2006], *Roy et al.* [2010] and *Tang and Lettenmaier* [2010].

[16] Our study uses quality-controlled forcing data from Phase 2 of the Distributed Model Intercomparison Project (DMIP2) (see <http://www.nws.noaa.gov/oh/hrl/dmip/2/>) [*Smith et al.*, 2010a], and, therefore, does not attempt to nudge meteorological forcings a day or more in advance of assimilation like *Huttunen et al.* [2005], *Udnaes et al.* [2007] and *Zaitchik and Rodell* [2009]. We apply a below-canopy allowance to observed fSCA during assimilation to account for below-canopy snow, while other techniques include the pixel canopy correction factor for scaling up the snow extent by *Dressler et al.* [2006]. Like our study, most previous assimilation studies were not ensemble-based. The exceptions were *Clark et al.* [2006] and *Thirel et al.* [2011], and also *Arsenault* [2011] which used an ensemble scheme in addition to direct insertion. Our

study is a first-cut direct insertion attempt at using and updating the depletion curve and model states, with development of ensemble-based techniques left for future work.

#### 4. Basins and Data Used

[17] As mentioned above, our study is conducted over the DMIP2 Western US basins and is forced with hourly DMIP2 temperature and precipitation on the  $\sim 4$  km Hydrologic Rainfall Analysis Project (HRAP) [Greene and Hudlow, 1982] grid. We assimilate MODIS satellite-based fSCAs into this distributed DMIP2-type model simulation. In addition to comparisons of modeled versus observed streamflow, modeled SWE values are also compared against SNODAS SWE analyses [Carroll et al., 2001; National Operational Hydrologic Remote Sensing Center (NOHRSC), 2004].

##### 4.1. DMIP2 Western Basins (North Fork American and the Nested East Fork Carson)

[18] The DMIP2 hydrological model intercomparison experiment provided a framework to test many distributed models with operational quality data, for meeting the needs of operational National Weather Service (NWS) forecasters. Figure 1 shows the two hydrologically complex DMIP2 Western basins located in the Sierra Nevada Mountains. Their hydrologic complexities include snow, orographic precipitation, rain-snow partitioning, forest canopies, steep slopes and other complex terrain features.

[19] Henceforth, the terms “Carson” and “American” refer to the East Fork of the Carson River and the North Fork of the American River, respectively. The basins lie on either side of the Sierra divide [Simpson et al., 2004], with the Carson on the eastern, leeward, rain-shadowed side draining south to north, and the American on the wetter, western, windward side draining westward. Average basin elevations are 2417 and 1270 m for the Carson and American, respectively, with respective ridgelines near 3400 and 2700 m. Although situated close geographically, their hydrologic regimes differ greatly: the high-altitude Carson is snow-dominated, while the lower-elevation American has rain and mixed rain-snow events. Annual precipitation ranges from 560–1244 mm over Carson and from 813–1651 mm over the American.

[20] Both basins are geologically dominated by the granodiorites of central Sierra Nevada, with additions from volcanic and metasedimentary rocks for Carson and American, respectively [Jeton et al., 1996]. The Carson has shallow sandy and clay soils, while American is characterized by clay loams and coarse sandy loams. Vegetation varies from subalpine and alpine conifer forests and meadows at the upper elevations of both basins, to chaparral-sagebrush rangelands in the lower elevations of the Carson, and pine-oak woodlands and shrub rangelands in the lower regions of the American. Based on the UMD vegetation continuous fields data (see <http://glcf.umd.edu/data/vcf/>), the Carson’s higher elevation grid cells that receive most of the snow have forest canopy coverage ranging from 65% to 70%, and the lower elevations have coverage ranging from 30% to 60%. The American’s forest canopy coverage has a more uniform value of approximately 73%. Both basins are largely unregulated [Jeton et al., 1996; Dettinger et al., 2004], although there do exist a few small reservoirs and diversions.

[21] While springtime snowmelt runoff dominates Carson streamflow overall, the largest peaks stem from rain-on-snow events. In contrast, about two-thirds of streamflow in the American stems from wintertime rainfall and snowmelt runoff, and less than one-third from springtime snowmelt runoff [Dettinger et al., 2004]. Hourly streamflow in the Carson is measured by two nested USGS instantaneous stream stage gauges: the downstream Gardnerville gauge 10-30900 in Nevada and the upstream Markleeville gauge 10-308200 in California. These gauges drain, respectively, 922 and 715 km<sup>2</sup>, while the American gauge 11-427000 at North Fork Dam 11-427000 in California drains 886 km<sup>2</sup>.

##### 4.2. MODIS MOD10A1 Fractional Snow Extent Product

[22] The fractional snow cover area (fSCA) is drawn from Collection 5 MOD10A1 500 m daily fSCA (see <http://modis-snow-ice.gsfc.nasa.gov>) [Riggs et al., 2006] obtained by the MODIS electro-optical sensor on the Terra spacecraft. The MOD10A1 fSCA calculation involves a statistical-linear equation [Salomonson and Appel, 2004, 2006] to the Normalized Difference Snow Index (NDSI). The assumed “truth” data for this equation were binary snow presence values from the Landsat-7 Enhanced Thematic Mapper-Plus (ETM+; see <http://landsat.gsfc.nasa.gov/>). Like MODIS, ETM+ also does not properly sense snow under forest canopy for the Sierra Nevada, but its finer 30 m resolution can lead to slightly more accuracy than the MOD10A1 fSCA.

[23] Aggregation of the MOD10A1 data to a spatially coarser resolution (e.g., our  $\sim 4$  km HRAP grid) can decrease confidence in the coarser estimates if any 500 m cloud covered pixels exist. In the 0.05° MOD10C1 MODIS fSCA product, the confidence index (CI) and the snow extent are the percentage of cloud-free pixels and binary snow pixels among all land pixels, respectively. MOD10A1’s mutually exclusive mapping of cloud and snow pixels means the MOD10C1 extent calculation assumes no snow under cloud pixels, whereas a possibly better assumption is that the proportion of snow-free land versus snow-covered land among the cloud-free pixels is also maintained among the cloud pixels. We accordingly calculate the CI but by using fSCA instead of binary snow values, where the coarser grid’s fSCA is the average of the cloud-free pixels’ fSCAs. The Land Information System software (LIS) [Kumar et al., 2006; Peters-Lidard et al., 2007] directly reads the MOD10A1 via our additional coded internal reader utilizing Hierarchical Data Format–Earth Observing System (HDF-EOS) library tools. The LIS integrates satellite- and ground-based observational data with advanced land modeling techniques to produce optimal fields of land surface states and fluxes. Our study assimilates fSCA values with a high CI value of 80% (compared to values of 50–80% in Andreadis and Lettenmaier [2006], 90% in Hall et al. [2010]). Lower CI thresholds have been used in other studies in an attempt to retain more information during snowfall when clouds are present (e.g., 6% by Rodell and Houser [2004] and Zaitchik and Rodell [2009]).

##### 4.3. SNODAS Snow Analysis Product

[24] The SNODAS [Carroll et al., 2001; NOHRSC, 2004] is a spatially distributed modeling and data assimilation framework which attempts to provide the best possible

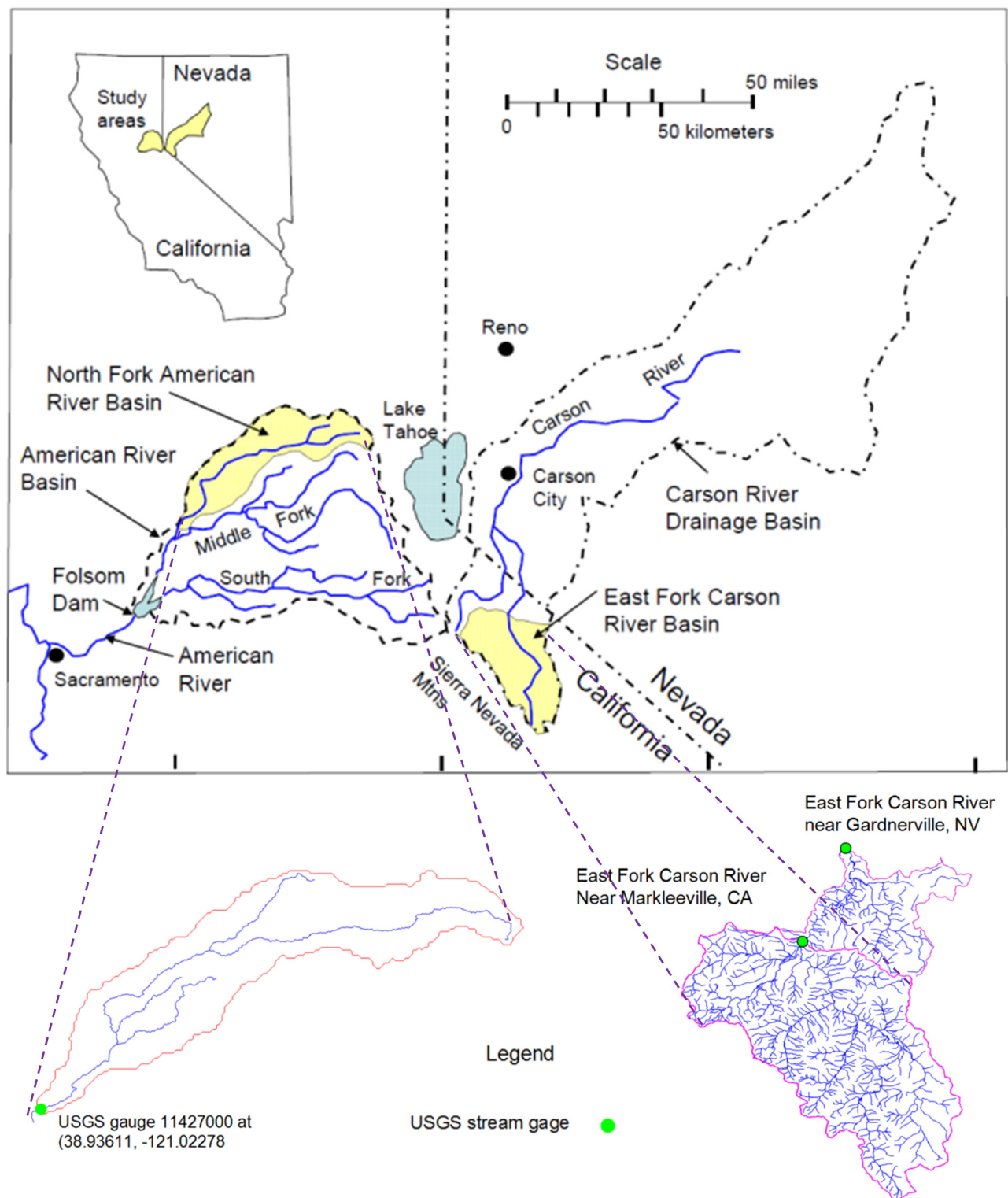


**Figure 1.** Overview of the DMIP2 Western basins used in this study (adapted from *Jeton et al.* [1996] and *Smith et al.* [2010b]) showing stream gauge locations.

physically consistent (i.e., snow energy and mass balance based) estimates of snow properties on a 1-km grid throughout the US and parts of Canada to support hydrologic modeling and analysis. It assimilates observations from ground stations,

satellites, and airborne passive gamma-ray sensors. These gamma-ray sensors may potentially sense snow better under the canopy in mountainous forests than do their electro-optical remote sensing counterparts (e.g., MODIS). Model forcings

includes downscaled fields from numerical weather prediction models, surface weather observations, satellite-derived solar radiation and radar-derived precipitation.

## 5. Model and Assimilation Methodology

### 5.1. NOAA OHD's Hydrology Component Models and Their Porting Into LIS

[25] The National Oceanic and Atmospheric Administration's Hydrology Laboratory Research Distributed Hydrologic Model (HL-RDHM) is an updated version of the Hydrology Laboratory-Research Modeling System (HL-RMS) [Koren *et al.*, 2004]. It includes gridded hydrological model features and components. To exploit LIS data handling and assimilation capabilities, we ported into LIS the following HL-RDHM components: the gridded forcing reader, the SNOW-17 snow model [Anderson, 1973, 2006], and the Sacramento Heat Transfer (SAC-HT) [Koren *et al.*, 2007; Burnash, 1995] surface water balance model. The hill- and channel-slope runoff routing postprocessor utilizes a physically based kinematic wave approach that provides unconditional stability [Reed, 2003; Koren *et al.*, 2004].

[26] Meteorological inputs are first passed to the SNOW-17 model which represents the snowpack as a relatively simple one-dimensional bulk layer with an associated water holding capacity. Rain-on-snow periods use energy balance-based melt computations, while nonrain (or negligible rain) periods utilize a temperature index equation. During subfreezing temperatures, a heat deficit function tracks the energy needed to return to an isothermal, or ripe, snowpack state. This deficit is a function of the temperature gradient between the snow surface temperature (the minimum of the air temperature and 0°C) and a computed snowpack antecedent temperature index. Liquid water storage calculations using the heat deficit ensure preferential refreezing of any surface melt or rain before adding to the liquid water storage and outflow (in contrast to Slater and Clark [2006] where contribution to liquid water storage or outflow is preferred to refreezing within the snow). Any excess water is lagged in time and attenuated during transmission through

the snowpack according to the ratio of the ice water equivalent and this excess water. SNOW-17 has 22 parameters (Table 1). The shape of the areal depletion curve (ADC) is described by 11 of these parameters, and the ADC and its adjustment during fSCA assimilation are described in a following section.

[27] Snowmelt from SNOW-17 and precipitation over snow-free areas force the SAC-HT water balance model. SAC-HT has upper and lower zone tension and free water storages representing a relatively thin upper layer, and a much thicker lower layer. The model simulates evaporation, saturation-excess infiltration, percolation, fast runoff response components (surface runoff and direct runoff from impervious surfaces), slower runoff responses (interflow, supplemental and primary base flow), and nonchannel subsurface outflow.

[28] A grid cell's drainage density parameter delineates conceptual overland flow plane hillslopes. SAC-HT hillslope fast response runoff drains into a conceptual channel having the cell diagonal as its maximum length. Hillslope slow response runoff enters the channel directly.

### 5.2. SNOW-17 Areal Depletion Curve and Direct Insertion Assimilation of fSCA

[29] Different areal depletion curve (ADC) types relate the fSCA to the current fraction of total seasonal runoff, the time of the year, degree-days, and the SWE. Common operational ADCs as used in SNOW-17 calculate fSCA from the modeled SWE (i.e., fSCA is diagnostic).

[30] For a given area, the general shape of such fSCA versus SWE ADCs is generally similar across years, reflecting the fairly high interannual consistency in the spatial variations of the relative snow amounts [e.g., Liston, 1999, 2004; Luce *et al.*, 1999; Luce and Tarboton, 2004; Anderson, 2006; Kolberg and Gottschalk, 2010; Homan *et al.*, 2011]. Many factors affecting accumulation and melt combine toward this year-to-year consistency, including temperature, storm type and direction, wind speed, cloudiness, dew-point temperature, topographical factors like elevation, slope and aspect, and vegetation [e.g., König and Sturm, 1998;

**Table 1.** SNOW-17 Parameter Values, Ranges, and Grid Scaling Factors<sup>a</sup>

Number	Parameter	Values/Ranges (Grid Scaling Factor)							Units
		GU <sup>b</sup>	GC <sup>b</sup>	MU or BU <sup>b</sup>	MC <sup>b</sup>	BC <sup>b</sup>	AU <sup>b</sup>	AC <sup>b</sup>	
1	SCF	1	0.75–1.5	1	1.07–1.25	1–1.15	0.75–1.15	Same <sup>c</sup>	–
2	MFMAX	0.5–1.29 [1]	0.45–1.6 [1]	0.5–1.2 [1]	0.54–1.18 [1.075]	0.54–1.18 [1]	0.51–1.71 [1]	0.51–1.71 [1.5]	mm/°C/(6 h)
3	MFMIN	0.2–0.5 [1]	0.08–0.53 [1]	0.2–0.4 [1]	0.08–0.53 [1]	0.08–0.53 [1]	0.08–0.53 [1]	0.08–0.53 [1.5]	mm/°C/(6 h)
4	UADJ	0.05	Same <sup>c</sup>	0.05	Same <sup>c</sup>	Same <sup>c</sup>	0–0.03	Same <sup>c</sup>	mm/mb/(6 h)
5	SI	500	Same <sup>c</sup>	500	Same <sup>c</sup>	Same <sup>c</sup>	999	Same <sup>c</sup>	mm
6 to 16	ADC	0.05, 0.15, 0.29, 0.41, 0.51, 0.60, 0.65, 0.68, 0.72, 0.76, 1.0	Same <sup>c</sup>	Same as GU	Same <sup>c</sup>	Same <sup>c</sup>	0.0, 0.1, 0.2, 0.3, 0.4, 0.5, 0.6, 0.7, 0.8, 0.9, 1.0	Same <sup>c</sup>	–
17	NMF	0.15	Same <sup>c</sup>	0.15	Same <sup>c</sup>	Same <sup>c</sup>	0.15	Same <sup>c</sup>	mm/°C/(6 h)
18	TIPM	0.06	0.05–0.1	0.06	0.05–0.1	0.05–0.1	0.1–0.2	Same <sup>c</sup>	1/(6 h)
19	PXTEMP	2	Same <sup>c</sup>	2	Same <sup>c</sup>	Same <sup>c</sup>	2	Same <sup>c</sup>	°C
20	MBASE	0	Same <sup>c</sup>	0	Same <sup>c</sup>	Same <sup>c</sup>	0	Same <sup>c</sup>	°C
21	PLWHC	0.03	Same <sup>c</sup>	0.03	Same <sup>c</sup>	Same <sup>c</sup>	0.05–0.3	Same <sup>c</sup>	–
22	DAYGM	0.2	0.1–0.3	0.2	0.1–0.3	0.1–0.3	0.3	Same <sup>c</sup>	mm d <sup>−1</sup>

<sup>a</sup>Parameter descriptions given in section VI of Anderson [2006].

<sup>b</sup>G = Gardnerville, M = Markleeville, B = Blind, A = American, U = Uncalibrated, C = Calibrated.

<sup>c</sup>Same as respective uncalibrated value/s.

Luce *et al.*, 1998; Deems *et al.*, 2008; Grünwald *et al.*, 2010; Rice *et al.*, 2010] (detailed review in Clark *et al.* [2011]). In the SNOW-17 ADC, the Snow Index (SI) parameter is the upper limit of the Areal Index  $A_i$ , which is itself the variable minimum seasonal SWE accumulation at 100% fSCA. So SI is the minimum areally averaged SWE above which fSCA is always at its maximum possible value (100%), and below which the fSCA is 100% or less depending on SWE and  $A_i$  [Anderson, 2006] (see SI limit in Figure 2a). At maximum fSCA, when  $A_i$  updates upward during the control run (i.e., nonassimilation) accumulation, the entire ADC instantaneously steepens. At nonmaximum fSCA, the ADC has an additional ‘new snow’ trajectory behavior when fSCA temporarily becomes 100% from an arbitrarily set  $0.2 \text{ mm hr}^{-1}$  minimum snowfall on a partially bare area. This 100% fSCA remains until an arbitrarily chosen value of 25% of this newly fallen snow melts, and then the trajectory linearly returns to the earlier prenew snow trajectory point on the ADC (Figure 2a).

[31] Our direct insertion technique is based on the NWS operational manual modification (MOD) of state variables [Anderson, 2002, 2006] called the Areal Extent of Snow Cover Change (.AESCCHNG). Note that this MOD notation differs from the MODIS MOD10A1 data. The .AESCCHNG preserves SWE by assuming no intrinsic SWE information in the observed fSCA. Assimilating fSCA gives different ADC trajectory alterations cases depending on observed fSCA relative to modeled values. These alterations change snow processes, SWE and timing of melt down the line, eventually impacting streamflow. The case depicted in Figure 2b shows the preassimilation (i.e., “Old”) SNOW-17 fSCA where the entire ADC is instantaneously able to steepen and flatten during both snow accumulation and melt phases. By comparison, the control run ADC continuously steepens and only during accumulation. Thus the observed fSCA instead of the  $A_i$  controls the trajectory change, i.e., fSCA is now prognostic as compared to being diagnostic in the control run. Figures 2c and 2d depict cases starting on the “new snow”

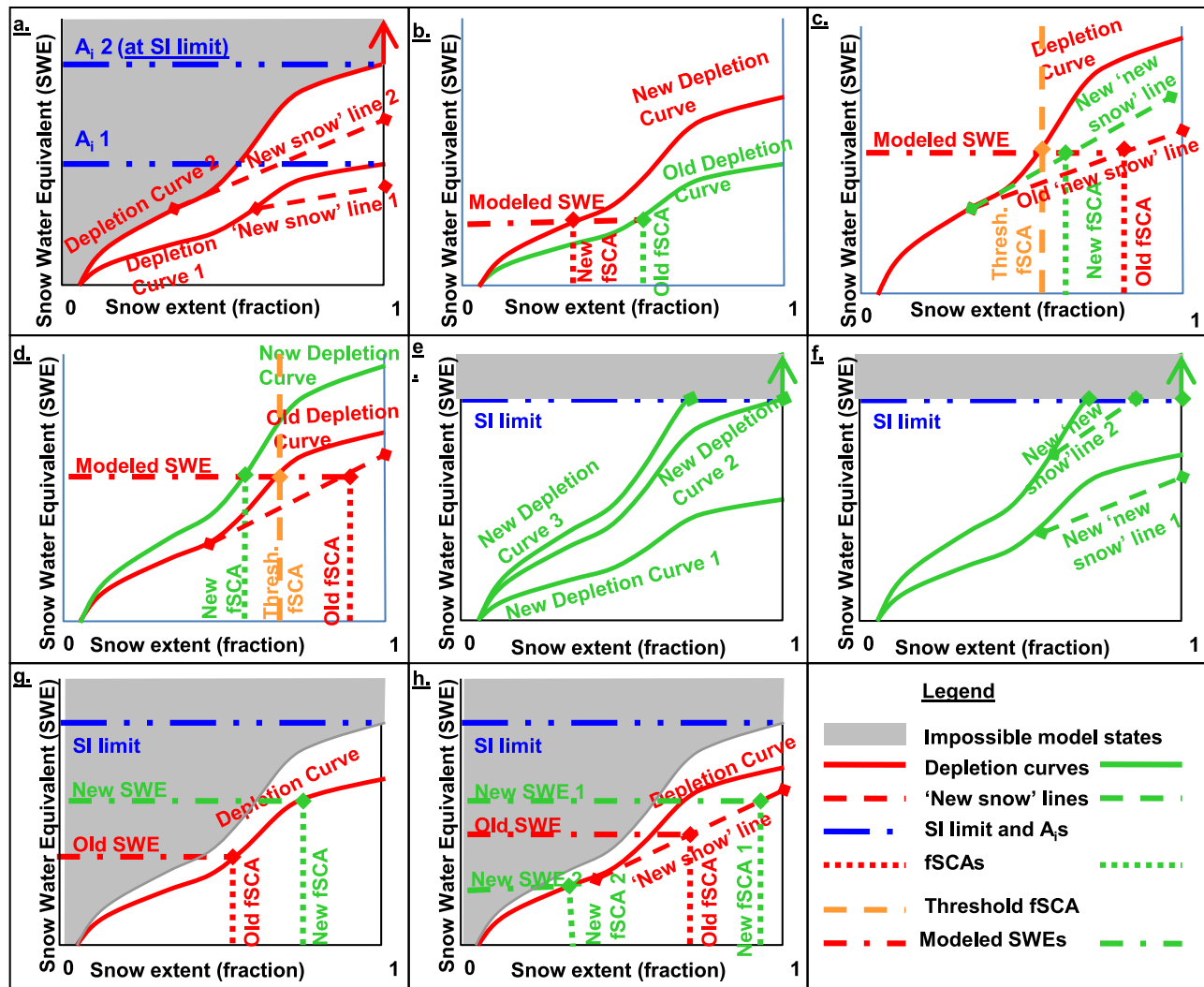


**Figure 2.** Graphical depiction of direct-insertion update cases using example ADCs and “new snow” lines in: (a) Control run; (b–d) .AESCCHNG Mod assimilating fSCA by attempting to preserve SWE; (e and f) Enhanced Mod where new fSCA = 1.0 enforced if SWE > SI; and (g and h) Runs assimilating fSCA to derived new SWE using the ADC.

line where .AESCCHNG adjusts either this line, or the ADC (i.e., new  $A_i$ ), depending on whether the assimilated fSCA is greater or less, respectively, than the fSCA corresponding to the SWE on the preassimilation ADC (i.e., see the dashed “Threshold fSCA” line in Figure 2 legend).

[32] Note that .AESCCHNG is used only in cases where both the modeled and observed fSCA are nonzero (i.e., mutually exclusive snow/no-snow cases between model and observations). Additionally, .AESCCHNG could allow a new  $A_i$  beyond the realistic upper limit of SI. In response to this, we simultaneously enhance .AESCCHNG to avoid this  $A_i$  upper limit problem and the inaction during the mutually exclusive snow/no-snow cases. This is accomplished by implementing an SI constraint when the SWE goes above SI to enforce the postassimilation fSCA at 100%, irrespective of the observed fSCA (Figures 2e and 2f). Similar to Rodell and Houser [2004] and Zaitchik and Rodell [2009], we handle the mutually exclusive cases of snow/no-snow through allowing ‘unavoidable’ alterations to the SWE (not shown): (1) For modeled extents at zero, we add SWE derived from nonzero observed fSCA and an ADC defined by  $A_i$  at 5 mm, and (2) For observed fSCA at zero, we remove existing modeled SWE.

[33] In addition to these .AESCCHNG-based runs that assume no intrinsic SWE information in the observed fSCA, we also test the opposite assumption that combines fSCA with the existing modeled ADC to reconstruct SWE (Figures 2g and 2h). This differs from the operational Water Equivalent Change (.WECHNG) MOD that adjusts the ADC using observed SWE.

### 5.3. Hydrological Model Parameterization, Including the Areal Depletion Curve

[34] Tables 1–3 lists the parameter names, corresponding values, ranges and scalar multipliers for the uncalibrated (*a priori*) and calibrated runs. The Carson, with two nested streamflow gauges (Figure 1), serves as the domain for two uncalibrated and three calibrated control runs. The extra calibrated control run makes use of the interior Markleeville gauge as a ‘blind’ streamflow simulation point testing

the Gardnerville domain calibrated parameters. The single American gauge has only one uncalibrated and one calibrated control run. The hitherto undetailed process of creating the uncalibrated and calibrated parameters occurred as part of the DMIP2 Western basins study [Smith *et al.*, 2010b], so is briefly outlined below for completeness.

[35] The SNOW-17 *a priori* values for MFMAX, MFMIN and MBASE are obtained by combining a derived energy-based temperature index snowmelt equation for spring snow pack with the SNOW-17 temperature index model, using available spatial physiographic data, and wind speed climate grids from the North American Regional Reanalysis (NARR) [Mizukami and Koren, 2008]. With the exception of the ADC, the remaining parameters were derived from lumped-calibrated values from the California Nevada River Forecast Center and knowledge of the local snowfall and wind climatologies. The SAC-HT *a priori* physically based parameters are derived from physiographic properties like soil texture and land cover [Koren *et al.*, 2000; Zhang *et al.*, 2011]. The routing *a priori* parameters are from DEM, land use and empirical equations based on channel hydraulic data [Koren *et al.*, 2000].

[36] In the manual American calibration process, the distributed *a priori* values are first scaled to match pre-existing calibrated lumped values. All scalar parameters are then adjusted to replicate observed hourly streamflow using the following sequential methodology for lumped models [Smith *et al.*, 2003]: Removal of major biases and errors, matching of SAC-HT base flows, general SNOW-17 calibration, further calibration to match in-situ observed SWE, matching of the faster responding surface runoff, and adjustment of routing parameters. Streamflow matching is done using visual comparison and multiple goodness-of-fit measures at different stages, e.g., base flow statistics, seasonal statistics, flow interval biases, run period accumulated error, overall bias and the modified correlation coefficient [McCuen and Snyder, 1975]. The Carson calibration is similar, except: (1) Parameters from two elevation zones in a preexisting lumped calibration give two corresponding zone fields (though single multipliers then

**Table 2.** SAC-HT Parameter Values, Ranges, and Grid Scaling Factors<sup>a</sup>

Number	Parameter	Values/Ranges (Grid Scaling Factor)							Units
		GU <sup>b</sup>	GC <sup>b</sup>	MU or BU <sup>b</sup>	MC <sup>b</sup>	BC <sup>b</sup>	AU <sup>b</sup>	AC <sup>b</sup>	
1	UZTWM	23–64 [1]	6.48–42.56 [1.5]	23–64 [1]	6.48–42.56 [2.225]	6.48–42.56 [1.5]	41–59 [1]	41–59 [1.218]	mm
2	UZFWM	21–54 [1]	30.97–73.75 [2.5]	38–54 [1]	13.48–42.97 [5]	44.99–63.93 [2.5]	29–53 [1]	29–53 [1.2]	mm
3	UZK	0.34–0.75 [1]	0.23–0.47 [0.475]	0.47–0.75 [1]	0.25–0.41 [0.475]	0.25–0.41 [0.475]	0.38–0.51 [1]	0.38–0.51 [0.7]	1 d <sup>−1</sup>
4	ZPERC	45.2–79.5 [1]	52.2–118.4 [0.875]	Same as GU	52.25–118.37 [0.5]	52.23–118.37 [0.875]	44.2–108 [1]	Same <sup>c</sup>	–
5	REXP	1.01–2.89 [1]	0.99–2.55 [1]	1.01–2.07 [1]	0.99–2.55 [1]	0.99–2.55 [1]	1.6–2.49 [1]	1.6–2.49 [0.95]	–
6	LZTWM	59–252 [1]	28.7–122.5 [0.825]	59–252 [1]	24.8–106.1 [1.0875]	28.67–122.47 [0.825]	92–248 [1]	92–248 [4.7]	mm
7	LZFSM	2.5–20.8 [1]	27.69–230.42 [1]	2.5–20.8 [1]	27.69–230.42 [1]	27.69–230.42 [1]	7.9–34.9 [1]	7.9–34.9 [8.5]	mm
8	LZFFM	15–194 [1]	23.44–187.55 [1]	89–194 [1]	85.52–186.43 [1]	85.52–186.43 [1]	46–191 [1]	46–191 [1.11]	mm
9	LZSK	0.14–0.26 [1]	0.04–0.07 [1]	0.18–0.26 [1]	0.04–0.07 [1.39]	0.04–0.07 [1]	0.14–0.18 [1]	0.14–0.18 [0.5]	1 d <sup>−1</sup>
10	LZPK	0–0.03 [1]	0–0.01 [1]	0–0.03 [1]	0–0.005 [1]	0–0.005 [1]	0–0.03 [1]	0–0.03 [0.29]	1 d <sup>−1</sup>
11	PFREE	0.01–0.46 [1]	0.02–0.45 [2]	0.01–0.18 [1]	0.03–0.45 [1.89]	0.03–0.45 [2]	0.08–0.3 [1]	0.08–0.3 [0.51]	–
12	PCTIM	0	Same <sup>c</sup>	0	Same <sup>c</sup>	Same <sup>c</sup>	0.003	Same <sup>c</sup>	–
13	ADIMP	0	0–0.2	0	0–0.2	0–0.2	0–0.25	Same <sup>c</sup>	–
14	RIVA	0	Same <sup>c</sup>	0	Same <sup>c</sup>	Same <sup>c</sup>	0.001	Same <sup>c</sup>	–
15	SIDE	0	Same <sup>c</sup>	0	Same <sup>c</sup>	Same <sup>c</sup>	0	Same <sup>c</sup>	–
16	RSERV	0.3	Same <sup>c</sup>	0.3	Same <sup>c</sup>	Same <sup>c</sup>	0.3	Same <sup>c</sup>	–

<sup>a</sup>Parameter descriptions given in Table 1 of Koren *et al.* [2004].

<sup>b</sup>G = Gardnerville, M = Markleeville, B = Blind, A = American, U = Uncalibrated, C = Calibrated.

<sup>c</sup>Same as respective uncalibrated values.

**Table 3.** Routing Parameter Values, Ranges, and Grid Scaling Factors<sup>a</sup>

Number	Parameter	Values/Ranges (Grid Scaling Factor)							Units
		GU <sup>b</sup>	GC <sup>b</sup>	MU or BU <sup>b</sup>	MC <sup>b</sup>	BC <sup>b</sup>	AU <sup>b</sup>	AC <sup>b</sup>	
1	SLOPH	0.13–0.5	Same <sup>c</sup>	0.22–0.5	Same <sup>c</sup>	Same <sup>c</sup>	0.09–0.3	Same <sup>c</sup>	–
2	DS	2.5	Same <sup>c</sup>	2.5	Same <sup>c</sup>	Same <sup>c</sup>	2.5	Same <sup>c</sup>	1 km <sup>–1</sup>
3	ROUGH	0.15	Same <sup>c</sup>	0.15	Same <sup>c</sup>	Same <sup>c</sup>	0.15	Same <sup>c</sup>	–
4	Q0CHN	0.1–1.59	Same <sup>c</sup>	0.11–1.34	Same <sup>c</sup>	Same <sup>c</sup>	0.72–2.86 [1]	0.7–2.86 [1.75]	m <sup>3</sup> /s/m <sup>2</sup> (2*QMCHN)
5	QMCHN	1.79	Same <sup>c</sup>	1.79	Same <sup>c</sup>	Same <sup>c</sup>	1.47 [1]	1.47 [0.8]	–

<sup>a</sup>Parameter descriptions given in Table 3.2 of the HL-RDHM user manual at [http://www.cbrfc.noaa.gov/present/rdhm/RDHM\\_3\\_0\\_0\\_User\\_Manual.pdf](http://www.cbrfc.noaa.gov/present/rdhm/RDHM_3_0_0_User_Manual.pdf).

<sup>b</sup>G = Gardnerville, M = Markleeville, B = Blind, A = American, U = Uncalibrated, C = Calibrated.

<sup>c</sup>Same as respective uncalibrated value/s.

both zones varied together), and (2) A mixture of manual and Simplified Line Search automated approaches [Kuzmin *et al.*, 2008] provides the final calibrated distributed values.

[37] A principal difference between our study's and DMIP2's uncalibrated Carson configuration is our nonzero SI value (versus the DMIP2 a priori SI value of zero). This change was essential, as a zero SI means only 0% or 100% values of fSCA are allowed, effectively reducing the fSCA information during assimilation to rule-based binary values as in Rodell and Houser [2004]. We instead use the DMIP2 calibrated SI (and associated ADC) for both calibrated and uncalibrated Carson runs. The DMIP2 uncalibrated zero SI is simplistic and reflects typical operational constraints on the assignment of SI and ADC. More broadly, where skill level or time available is not optimal, a simplistic SI assignment can be either (1) a 0 as mentioned above where the basin-wide fSCA becomes the percent of pixels with snow presence, or (2) a very high value like 9999 or 999 mm (e.g., 999 for American) that is always above existing SWE values so that bare ground is exposed immediately as melt starts. This second option is useful when future plans include refined SI calibration using multiple years of

high-snow data. Snowmelt and streamflow can be very sensitive to SI [Anderson, 2002]. For example, a low (high) SI gives corresponding lower (higher)  $A_i$ , higher (lower) fSCA derived off the depletion curve, higher (lower) snowmelt and higher (lower) streamflow.

[38] Similar to the simplistic SI assignment mentioned above, all American runs feature a simplistic straight line ADC assignment [Anderson, 2002], which performed well in DMIP2. However, for the Carson, the more sophisticated DMIP2-calibrated ADC was derived using previously established ADCs for well-studied, calibrated basins in the same region, in addition to information on terrain, vegetation, climatic conditions, satellite measurements, and any available fSCA (e.g., from the National Operational Hydrologic Remote Sensing Center).

#### 5.4. Snow Assimilation Allowance Under Dense Forest Canopy During Snow Melt

[39] Figure 3 (top) shows a bird's-eye nadir view of satellite-sensed fSCA (fSCA<sub>satellite</sub>) components in a conceptual grid square area, based on vertically projecting forest canopy and snow extents onto the ground surface: areas

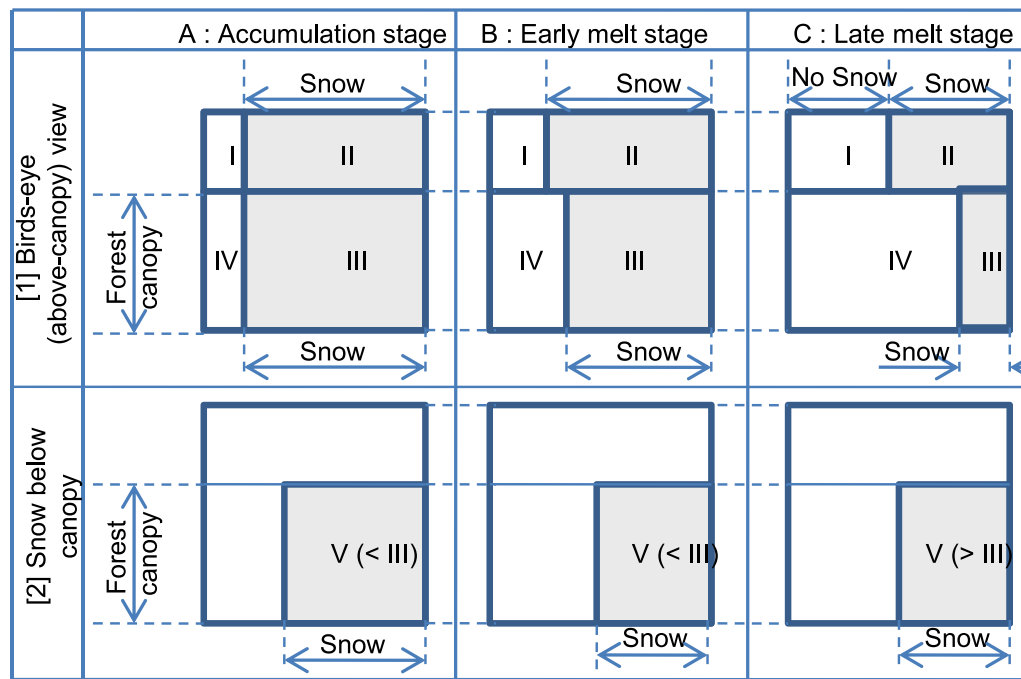


**Figure 3.** Components of a satellite's electro-optically sensed snow extent value (top) in a conceptual (SNOW-17) + (SAC-HT) grid square, and (bottom) of below-canopy portion V that may be undetected.

I, II, IV and III denote no-canopy no-snow, no-canopy snow, canopy no-snow, and canopy snow, respectively. Values IV and III are based above the canopy. The total no-canopy and canopy areas are  $(I + II)$  and  $(IV + III)$ , respectively. Satellite sensors miss the below-canopy snow component V of the true fSCA ( $fSCA_{true}$ ) in Figure 3 (bottom). As such,  $fSCA_{satellite}$  is the sum of only II and III (II and III values are not separately given). During accumulation (Figure 3a), snow covers almost the entire grid square (i.e., I and IV are 0 or negligible), with the above-canopy amount (III) usually greater than the below-canopy amount (V), indirectly making  $fSCA_{satellite}$  equal to  $fSCA_{true}$ . Assimilating fSCA in this stage is done without any melt time allowance, contrary to what is done during the snow melt phase described below.

[40] We assume that the late melt stage roughly occurs when the above-canopy snow III has become less than the below-canopy V (Figure 3c). Since the temporal variation of II, III and V values are unknown under existing model and data constraints, we provide an unavoidably wide melt-period upper allowance equal to the forest canopy area on the  $fSCA_{satellite}$  to be assimilated (here forth denoted the “UnsensedSnow” effect). Note that the ideal allowance should be a reduced value of IV (or canopy area minus the III value) instead of the entire canopy area, but this reduction is unachievable since the III value is not separately known. The assimilation is limited to constraining postassimilation fSCA to outside this allowance-included range bounded by  $fSCA_{satellite}$  and  $(fSCA_{satellite} + \text{canopy area})$ . So when preassimilation modeled fSCA ( $fSCA_{model}$ ) is greater than the  $(fSCA_{satellite} + \text{canopy area})$  upper bound, the assimilation process reduces it to equality with that bound: the assimilation inaccuracy is the entire canopy area minus the difference between above-canopy III and below-canopy V. And when the preassimilation  $fSCA_{model}$  is less than the  $fSCA_{satellite}$  lower bound, the assimilation process increases it to the  $fSCA_{satellite}$  value: the assimilation inaccuracy is the difference between III and V.

[41] During early melt periods assumed to occur when the above-canopy snow III is greater than the below-canopy V (Figure 3b), an accumulation period-type assimilation without allowance seems suitable. However, since the timing of exact transition between early and late melt is not known under current model and data constraints (or when the relative dominance between III and V switches), we again implement a late melt period-style allowance. So when preassimilation  $fSCA_{model}$  is greater than the  $(fSCA_{satellite} + \text{canopy area})$  upper bound and the assimilation process reduces it to equality with that bound, the assimilation inaccuracy increases: it is now the canopy area plus the difference between above-canopy III and below-canopy V. For the case where the preassimilation  $fSCA_{model}$  is less than the  $fSCA_{satellite}$  lower bound, direct insertion assimilation inaccuracy is absent. Note that this entire first-cut approach violates a SAC-HT evapotranspiration demand calculation assumption that the snow areal proportion is the same in the canopy and no-canopy areas, a shortcoming that future refinements to the assimilation technique will address.

### 5.5. Description of the Direct-Insertion Assimilation Simulations

[42] All simulations span September 1995 to September 2006, mirroring the DMIP2 simulation period. Data

assimilation starts when MODIS fSCA becomes available (March 2000 for Terra MODIS), and we stress that a long spin up period is not required for our application. Thus six complete water years (WYs) (Octobers to Septembers) are available for evaluating the assimilation procedure (WYs 2001–06). The SNODAS data series commences in October 2003, providing only three WYs for SWE comparison (WYs 2004–06). Assimilation results for the SNODAS 3-WY period subset are similar to the 6-WY values and not reported. Table 4 lists the multiple runs. The control run corresponds to Figure 2a, the Mod assimilation run A to Figures 2b–2d, the enhanced Mod runs B and C to Figures 2e and 2f, and the SWE-recreation assimilation run D to Figures 2g and 2h. The uncalibrated control run serves as the baseline against which to judge the performance of the uncalibrated assimilation runs’ suite, and of an extra calibrated control run (denoted by Z) against which this suite can be compared. Note that runs B and C differ from A in having addressed the  $A_i$  upper limit and snow/no-snow issues (see section 5.2).

### 5.6. Assimilation Performance Evaluation Measures

[43] We compute event-based and continuous measures. Events considered are an evaluation period subset of DMIP2 events. We adapt DMIP’s event-based improvement measures [Smith *et al.*, 2004] to calculate streamflow error improvement from assimilation, against the control runs (runs here are spatially distributed). These measures include: flood runoff improvement, peak flow improvement and peak time improvement (see Appendix A, equations (A1)–(A3)). We also construct similar additional performance measures where improvement is calculated as a percent of the control run residual values instead of the observation values (see Appendix A, equations (A4)–(A6)): we henceforth specifically call these ‘residual improvement measures’ as compared to the former ones called ‘improvement measures’. These residual improvement measures are more relevant for determining how much the deviation of the control values from the observations is reduced by the assimilation, especially where these control value deviations, and so improvement measure values are low. In other words, where the residual improvement measure is a high  $y$  %, a low improvement measure at  $x$  % can theoretically improve to a value of only around  $x*(100/y)$  % when the assimilation results exactly match observations. This  $x*(100/y)$  % may still be of the same order as  $x$  %, indicating little available room for improvement.

**Table 4.** Descriptions and Notations Used for Assimilation Runs and Calibrated Control Run Compared Against Uncalibrated Control

Run	Run Description	Short Description
A	Operational .AESCCHNG Mod assimilating MODIS snow extents	MODIS: Mod
B	Enhanced Mod assimilating MODIS without allowance for snow under forest canopy	MODIS: No UnsensedSnow
C	Enhanced Mod assimilating MODIS with allowance for snow under forest canopy	MODIS: UnsensedSnow
D	MODIS assimilation updating SWE with allowance for snow under forest canopy	MODIS To SWE: UnsensedSnow
Z	Calibrated control run (for calculating improvement against uncalibrated control)	—

[44] Time-continuous streamflow improvement measures for a multiple water year (WY) period are computed as the average of corresponding single WY values. So streamflow bias improvement and streamflow bias residual improvement are the respective equivalents of the above mentioned event-based measures concerning flood runoff (see Appendix A, equations (A1) and (A4)). We also calculate the assimilation run's modified correlation coefficient and its improvement over the control run (equations (A7) and (A8)). Next, we calculate the percent of time steps where the assimilation run is better than the control run, and the streamflow residual improvement that occurs within those time steps (equations (A9) and (A10)).

[45] We also use time-continuous SWE improvement measures to assess basin-mean SWE. These are the SWE bias improvement, SWE bias residual improvement, SWE centroid date improvement and SWE centroid date residual improvement (equations (A11)–(A14)). Note that possible limitations of SNODAS SWE (very few gamma-ray flights per melt season, etc.) can mean that conclusions based on the SWE measures' values are possibly "weaker" and so used more for comparison than for evaluation.

## 6. Analysis of Results

[46] Figure 4 shows example melt season time series for the uncalibrated Carson. Run B SWE and streamflow decrease much faster (Figures 4b and 4c), due to MODIS fSCA values decreasing to 0. This behavior is irrespective of calibration or basin, and clearly shows the importance of allowance for below-canopy snow in satellite-based fSCA assimilation during melt. Figures 4d–4f plot monthly mean streamflow residual improvement against observed streamflow, confirming that the crucial melt season has well-performing assimilation time steps for some runs.

[47] We do not list peak timing measure values: though residual improvements ( $RI_t$ ) can be substantial, the corresponding actual improvements ( $I_t$ ) are too low to be meaningful. This means that the observed timing is already well-reproduced here, even for the uncalibrated control. Values for all other measures are in Table 5 and Figure 5. Immediately noticeable is that while some uncalibrated run streamflows do show improvement, the calibrated run streamflows mostly degrade, sometimes by a large amount. The unavoidable allowance-related inaccuracy in our assimilation compromises the combination of detailed physics representations and accurate satellite fSCA (in addition to a well-calibrated ADC) that is required to improve streamflow. For the calibrated Carson example, this inaccuracy is likely larger than the difference between the preadjustment fSCA<sub>model</sub> and the fSCA<sub>true</sub>, leading to degraded streamflow. The opposite is true for the well-performing uncalibrated Carson runs. We assume an improvement as significant or substantial if the percentage value for observation-related improvement measures (e.g.,  $I_y$ , not the residual improvement measure  $RI_y$  in Appendix A is above five. This criterion cannot assign significance to the SWE centroid date measures since  $I_c$  is in units of days. Hereafter, we discuss uncalibrated run results relevant to ungauged basins.

[48] The uncalibrated Carson run A ("MODIS: Mod") actually performs better than the control for SWE-related  $RI_W$ ,  $I_W$ ,  $RI_C$  and  $I_C$  as depicted in Table 5, but displays

consistent degradation against the control run for all streamflow-related measures  $RI_y$ ,  $I_y$ ,  $RI_{mod}$ , and  $r_{mod}$ , and low  $B_t$  values. This apparent discrepancy is explained through visual examination of the high-biased SWE in uncalibrated run A which fails to completely melt off during the summer (not shown): since SWE in the control and in other assimilation runs is mostly under-biased against SNODAS, higher SWE values from assimilation can be closer to observations and give a false impression of performance improvement (if streamflow scores are ignored).

[49] SWE improvement measures  $RI_W$ ,  $I_W$ ,  $RI_C$  and  $I_C$  in Table 5 consistently improve from run C ("MODIS: UnsensedSnow") to D ("MODIS To SWE: Unsensed Snow") regardless of basin or parameter calibration (not ADC calibration). This indicates that fSCA<sub>satellite</sub> recreates SWE instantaneously using the ADC better than through long-term ADC trajectory changes.

[50] The only assimilation run where a significant and consistent improvement occurs in both SWE and streamflow is the best-performing uncalibrated Carson run D ("MODIS To SWE: UnsensedSnow"). Corresponding SWE improvement measures  $RI_W$  and  $I_W$  are 45% and 9%, respectively (i.e., the average of the italicized ranges 42–48% and 8–10% in Table 5). Similarly, Table 5 run D values for  $RI_C$ ,  $I_C$ , streamflow  $RI_y$  and  $I_y$  are 28% (from 27–29%), 3.5 days (from 3.4–3.7 days), 68% (from 64–72%) and 17% (from 16% to 18%), respectively. Although the flood  $I_y$  and  $I_p$  values look significant for Gardnerville, their values for the SNODAS-available 3-year subperiod fall below the arbitrary 5% threshold. The uncalibrated Carson run D also does not degrade performance in terms of correlation (Figure 5), and features a high percentage of time when its streamflow is better than the control run ( $B_t \sim 70\%$ ). Run D likely performs better than runs A–C for the snow-dominated Carson because the below-canopy snow allowance supports better updates that instantaneously use the well-calibrated ADC to promptly propagate fSCA values into better SWE values. This leads to better runoff and streamflow (dominated by springtime snowmelt runoff) from the large snowpack. Note that the performance of this uncalibrated Carson run D is close to that of the calibrated run Z across all improvement measures.

[51] Unlike the Carson wherein uncalibrated run D was the consistent best performer, attempts to select a similar run for the American are inconclusive. Uncalibrated run D is generally best in terms of SWE bias (Table 5 highlighted values are 25% and 10% for  $RI_W$  and  $I_W$ , respectively). However, uncalibrated run B is best in terms of streamflow. Corresponding streamflow bias measures  $RI_y$  and  $I_y$  show strong improvement with respective values of 81% and 22%. By contrast, flood runoff and flood peak improvement values are modest: flood  $RI_y$ , flood  $I_y$ ,  $RI_p$  and  $I_p$  are 8%, 6%, 6% and 8%, respectively. The mixed rain-on-snow regime which characterizes the American leads to springtime snowmelt from snowpacks that are thinner than those of the Carson, and that account for less than one-third of the yearly runoff. Two-thirds of the annual runoff occurs earlier in the year from wintertime rainfall, where the assimilation allowance-related uncertainty is much higher than that in the Carson where the dominant runoff occurs toward the late melt season (refer to section 5.4). The difference in performance ranks when judging against SWE and

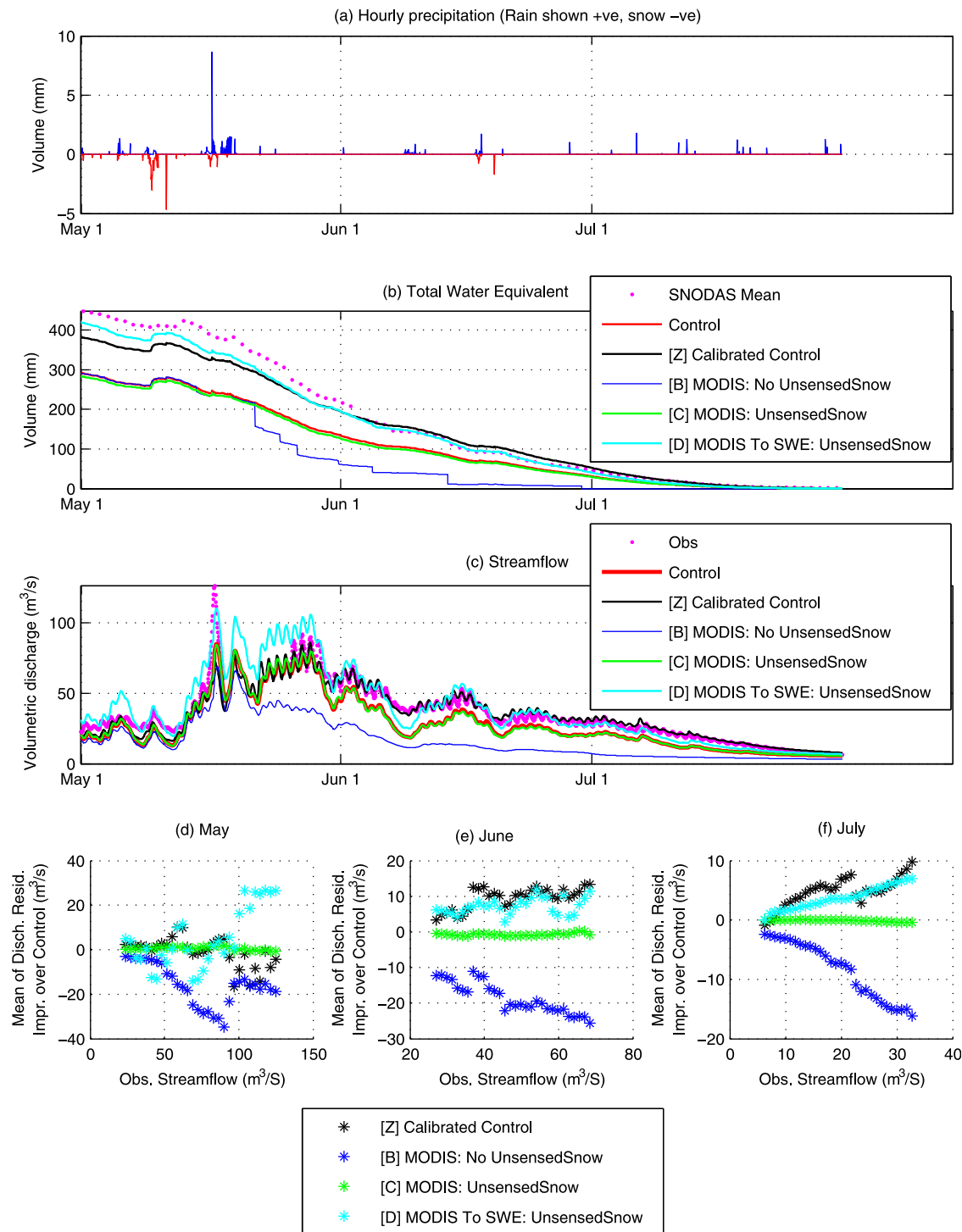


**Figure 4.** (a–c) Example precipitation, SWE, and streamflow plots: uncalibrated Carson runs for May–July 2005 springtime melt season. (d–f) Corresponding monthly plots of mean of discharge residual improvement (by assimilation) against observed streamflow.

streamflow may indicate the presence of SNODAS SWE bias in such mixed rain-on-snow basins.

## 7. Discussion and Recommendations for Future Work

[52] Improving modeled streamflow through assimilation of satellite-measured snow area is an important research

contribution [Andreadis and Lettenmaier, 2006; Simpson *et al.*, 2004]. We attempt this for the hydrologically challenging example of two Western US mountainous, densely forested basins (one snow-dominated and one rain- and snow-dominated) used in DMIP2. We apply a cautious below-canopy fSCA allowance during fSCA assimilation to avoid degrading simulated streamflow due to the lack of below-canopy measurements in the satellite fSCA product.

**Table 5.** Performance Improvement Values<sup>a</sup>

Outlet	Uncalibrated					Calibrated			
	Run A	Run B	Run C	Run D	Run Z	Run A	Run B	Run C	Run D
<i>RI<sub>w</sub> (%)</i>									
Gardnerville	<b>26</b>	−18	−5	<b>42</b>	<b>67</b>	−1113	−57	−16	10
Markleeville	<b>37</b>	−18	−7	<b>48</b>	<b>67</b>	−1288	−5	−7	0
Blind	<b>37</b>	−18	−7	<b>48</b>	<b>66</b>	−1046	−75	−3	10
American	−403	−3	−5	<b>25</b>	−12	<b>26</b>	−1	−7	<b>34</b>
<i>I<sub>w</sub> (%)</i>									
Gardnerville	<b>5</b>	−4	−1	<b>8</b>	<b>13</b>	−75	−4	−1	1
Markleeville	<b>8</b>	−4	−1	<b>10</b>	<b>14</b>	−88	0	0	0
Blind	<b>8</b>	−4	−1	<b>10</b>	<b>14</b>	−73	−5	0	1
American	−153	−1	−2	<b>10</b>	−4	<b>11</b>	0	−3	<b>15</b>
<i>RI<sub>c</sub> (%)</i>									
Gardnerville	78	−37	−8	29	25	45	−63	−1	12
Markleeville	73	−40	−9	27	20	48	−55	0	7
Blind	73	−40	−9	27	24	46	−63	−2	11
American	−3	−242	−21	−3	−234	64	−42	−21	49
<i>I<sub>c</sub> (Days)</i>									
Gardnerville	10.1	−4.8	−1.0	3.7	3.2	4.4	−6.1	−0.1	1.1
Markleeville	9.1	−5.0	−1.1	3.4	2.5	4.8	−5.5	0.0	0.7
Blind	9.1	−5.0	−1.1	3.4	3.0	4.4	−6.0	−0.2	1.1
American	−0.1	−8.6	−0.7	−0.1	−8.3	7.6	−4.9	−2.5	5.8
<i>RI<sub>y</sub> (%) Streamflow</i>									
Gardnerville	−122	−159	7	<b>72</b>	<b>71</b>	−462	−558	23	−100
Markleeville	−86	−111	8	<b>64</b>	<b>90</b>	−1277	−1458	4	−249
Blind	−86	−111	8	<b>64</b>	<b>83</b>	−773	−881	−14	−64
American	<b>53</b>	<b>81</b>	5	1	<b>81</b>	−72	−325	22	−45
<i>I<sub>y</sub> (%) Streamflow</i>									
Gardnerville	−26	−34	2	<b>16</b>	<b>15</b>	−29	−35	1	−6
Markleeville	−25	−32	2	<b>18</b>	<b>26</b>	−36	−41	0	−7
Blind	−25	−32	2	<b>18</b>	<b>24</b>	−38	−43	−1	−3
American	<b>14</b>	<b>22</b>	1	0	<b>22</b>	−4	−17	1	−2
<i>RI<sub>y</sub> (%) Flood</i>									
Gardnerville	−99	−92	−1	<b>19</b>	<b>28</b>	−185	−155	−2	7
Markleeville	−150	−132	3	<b>33</b>	<b>29</b>	−255	−161	−1	18
Blind	−150	−132	3	<b>33</b>	16	−238	−183	−4	10
American	0	<b>8</b>	3	0	<b>81</b>	−2	16	3	0
<i>I<sub>y</sub> (%) Flood</i>									
Gardnerville	−27	−25	0	<b>5</b>	<b>7</b>	−36	−30	0	1
Markleeville	−27	−24	0	<b>6</b>	<b>5</b>	−33	−21	0	2
Blind	−27	−24	0	<b>6</b>	3	−36	−28	−1	2
American	0	<b>6</b>	2	0	<b>60</b>	0	2	0	0
<i>RI<sub>p</sub> (%)</i>									
Gardnerville	−110	−104	−2	<b>26</b>	12	−159	−132	−2	5
Markleeville	−126	−111	2	<b>34</b>	<b>32</b>	−216	−131	−2	10
Blind	−126	−111	2	<b>34</b>	19	−201	−152	−3	7
American	2	<b>6</b>	<b>5</b>	0	<b>78</b>	6	14	3	2
<i>I<sub>p</sub> (%)</i>									
Gardnerville	−29	−28	−1	<b>7</b>	3	−37	−31	0	1
Markleeville	−28	−25	0	<b>8</b>	<b>7</b>	−33	−20	0	2
Blind	−28	−25	0	<b>8</b>	4	−36	−28	−1	1
American	2	<b>8</b>	<b>6</b>	0	<b>95</b>	2	4	1	1

<sup>a</sup>See Table 4 for run notations. Bold values are (assumed) significant improvements, italicized values are individually mentioned in sections 6 and 7.

The presence or absence of this allowance is one factor which differentiates the suite of direct-insertion assimilation runs presented in this study.

[53] Compared to the impacts of SWE assimilation noted in other studies, the information content in observed fSCA can be generally modest toward improving streamflow

simulations, especially over densely forested mountainous domains. Our study found fSCA assimilation mostly degraded streamflow for already well-performing calibrated runs where an accurate combination of model and data is required. This is because the below-canopy allowance inherently introduces an inaccuracy into the simulation that is

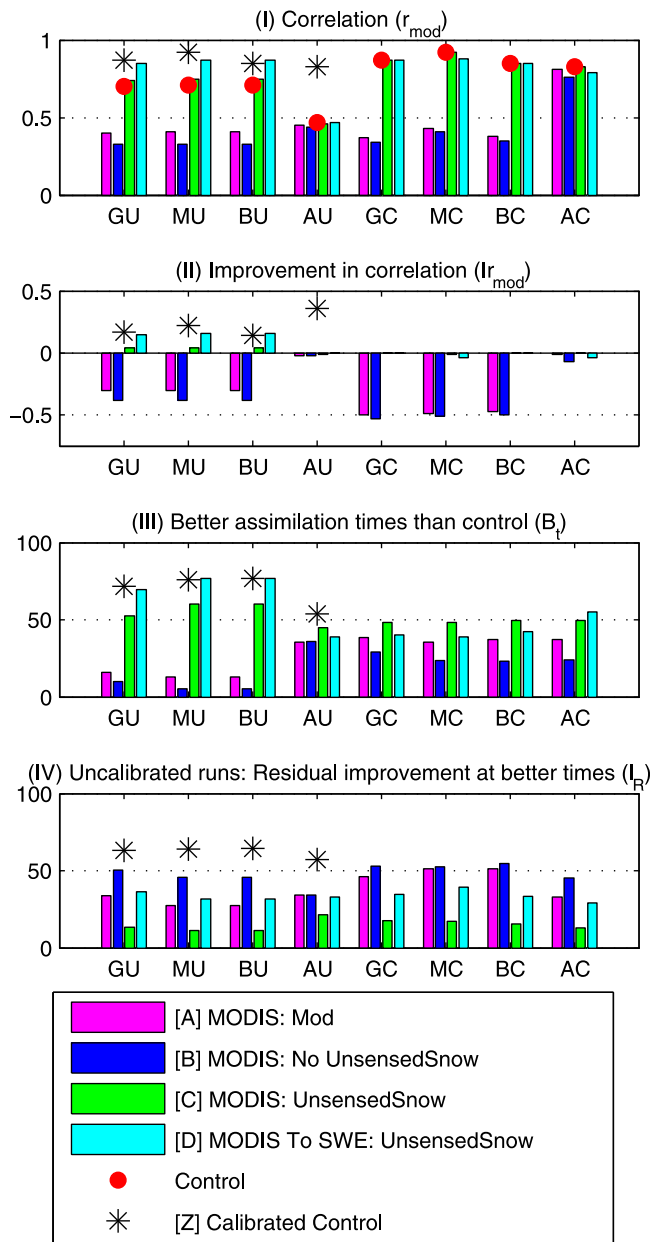


**Figure 5.** Correlation with observations, improvement in correlation over control, percent times when assimilation run streamflow better than control, and corresponding % residual improvement (Legend for 2-letter  $x$  axis tick label: G = Gardnerville, M = Markleeville, B = Blind, A = American, U = Uncalibrated, C = Calibrated).

likely more than the distance of preadjustment modeled fSCA ( $fSCA_{model}$ ) from the true value ( $fSCA_{true}$ ). However, for uncalibrated runs, though the SNOW-17/SAC-HT control run produces reasonably good streamflow performance, fSCA assimilation still leads to: (1) substantial to major improvements (64–81%) in streamflow volume as a percentage of the control run residuals (or distance from observations), and (2) minor improvements (16–22%) in streamflow volume as a percentage of observed values. The apparent difficulty in achieving multiobjective (i.e., all aspects of streamflow and SWE) improvement is similar to that seen in

earlier studies such as *Thirel et al.* [2011] where application of an ensemble Kalman filter (EnKF) led to improved timing of snow extent depletion but degraded streamflow. These challenges notwithstanding, the direct insertion technique assessed in this study has the potential to benefit applications over ungauged basins (coming close to the impact that calibration has on model performance), especially for snow-dominated basins where significant streamflow occurs during the spring.

[54] Comparing this study's results against those of earlier studies is generally hampered by those studies having either non-normalized objective functions like root mean square error, or inappropriate normalized objective functions (e.g., *Roy et al.* [2010] use the Nash coefficient with the oft-used mean-of-observations benchmark rather than with more appropriate benchmarks like calendar day or climatology as explained by *Schafeli and Gupta* [2007]). Where comparable, our results are at least of the same order. For example, *Thirel et al.* [2011] employ both the ensemble Kalman filter (EnKF) and particle filter techniques on flatter basins, and their Table 3 MODIS assimilation results show the discharge score ratio bias changing from 0.13 for the control run to 0.09 for the assimilation. This means that their streamflow volume residual bias improvement ( $RI_v$ ) is  $100 \times (0.13 - 0.09) / 0.13 = 31\%$  and their streamflow volume bias improvement ( $I_v$ ) is  $100 \times (0.13 - 0.09) = 4\%$ . Our corresponding values for the uncalibrated Carson and American simulations are 68% and 81%, respectively, for  $RI_v$ , and 17% and 22%, respectively, for  $I_v$  (see respective italicized values of 72–64%, 81%, 16–18% and 22% in Table 5). We also reran all the simulations reported in this paper with a lower (i.e., worse) confidence index acceptance threshold of 6% for the MODIS data [*Rodell and Houser*, 2004; *Zaitchik and Rodell*, 2009] and found that the conclusions remain valid with only a negligible degradation in the results.

[55] In practice, deciding on an appropriate run configuration based on our study suite will depend on the basin's characteristics such as whether it features dense or sparse forest canopy, whether the majority of streamflow occurs during wintertime or springtime etc. Consideration of, and adjustment for, additional factors such as the time of the year, the ongoing stage of snow season accumulation or depletion, and whether the basin is snow-dominated or has mixed rain-on-snow events may also prove beneficial. For example, the American basin features significant wintertime streamflow, possibly coinciding with times when the intercepted snow extent and the amount on the canopy are greater than the below-canopy amount. In this situation, it could be advantageous to have the assimilation procedure switch off the below-canopy snow allowance during wintertime streamflow/snow depletion, but activate it during springtime snow depletion. This allowance for prolonged below-canopy snow [e.g., *Musselman et al.*, 2008], missed by satellite instruments, is crucial when modeling the springtime melt period (Figures 5b and 5c).

[56] Additionally, while the accurate determination of the timing of the movement of snow from the canopy downward to the ground would be vital in the selection of the proper assimilation method, our snow model (and most current hydrology models) do not include detailed canopy, snow and optical radiative transfer physics. We believe that

such detailed process-oriented parameterizations providing information on the snow extent above and below the canopy are the way forward for improving real-time streamflow simulations. It is possible that inclusion of such processes would negate the need for calibrating the areal depletion curve.

[57] In addition to more detailed process representation, additional ways to improve assimilation results involve the data (satellite-derived MODIS). The overall quality of ingested snow data can be increased by switching off the assimilation of lower satellite-observed values of fSCA (like those below 25% that typically have errors, *Riggs et al.* [2006]). Another way to use the distributed data connected to the assimilation technique is through joint spatial assimilation of the distributed extent values. *Kolberg et al.* [2006] reported on such improvements judged against fully distributed assimilation by *Kolberg and Gottschalk* [2006]. Joint spatial assimilation is possible and is a focus of ongoing work for the model used in our study. In such over-constrained problem involving the pixel and basin values, we are implementing a SWE equilibrium achievement between the individual and joint snow extents, SWEs and the depletion curve for robustness and hydrologic consistency.

[58] Assimilation results here could be further improved using better techniques to measure and differentiate precipitation into rain and snow, e.g., the vertically pointing radar-estimated bright-band height [*Lundquist et al.*, 2008]. Finally, better results are possible for hydrologically less complex basins (the vast majority of basins, which feature gentler slopes or less forest canopy), given that improvements were possible even in our challenging scenario study.

## Appendix A

[59] (1) Flood runoff improvement and (2) streamflow bias improvement ( $I_y$ , %: streamflow improvement measure):

$$I_y = \frac{\sum_{i=1}^N (|Y_{o,i} - Y_{c,i}| - |Y_{o,i} - Y_{a,i}|)}{N \cdot Y_{o,avg}} 100 \quad (A1)$$

where  $Y_{o,i}$ ,  $Y_{c,i}$ , and  $Y_{a,i}$  are the runoff volumes of observations, control run, and assimilation run, respectively, for the  $i$ th flood or water year (WY),  $Y_{o,avg}$  is the average observed flood event runoff volume for  $N$  flood events or WYs.

[60] Peak flow improvement ( $I_p$ , %: streamflow event-based measure):

$$I_p = \frac{\sum_{i=1}^N (|Q_{po,i} - Q_{pc,i}| - |Q_{po,i} - Q_{pa,i}|)}{N \cdot Q_{po,avg}} 100 \quad (A2)$$

where  $Q_{po,i}$ ,  $Q_{pc,i}$ , and  $Q_{pa,i}$  are the peak discharges of observations, control run, and assimilation run, respectively, for the  $i$ th event,  $Q_{po,avg}$  is the average observed peak discharge for  $N$  events.

[61] Peak time improvement ( $I_t$ , hrs: streamflow event-based measure):

$$I_t = \frac{\sum_{i=1}^N (|T_{po,i} - T_{pc,i}| - |T_{po,i} - T_{pa,i}|)}{N} \quad (A3)$$

where  $T_{po,i}$ ,  $T_{pc,i}$ , and  $T_{pa,i}$  are the time (hrs) of observations, control run and assimilation run, respectively, for the  $i$ th peak.

[62] (1) Flood runoff residual improvement and (2) streamflow bias residual improvement ( $RI_y$ , %: streamflow measure):

$$RI_y = \frac{\sum_{i=1}^N (|Y_{o,i} - Y_{c,i}| - |Y_{o,i} - Y_{a,i}|)}{\sum_{i=1}^N |Y_{o,i} - Y_{c,i}|} 100 \quad (A4)$$

[63] Peak flow residual improvement ( $RI_p$ , %: streamflow event-based measure):

$$RI_p = \frac{\sum_{i=1}^N (|Q_{po,i} - Q_{pc,i}| - |Q_{po,i} - Q_{pa,i}|)}{\sum_{i=1}^N |Q_{po,i} - Q_{pc,i}|} 100 \quad (A5)$$

[64] Peak time residual improvement ( $RI_t$ , %: streamflow event-based measure):

$$RI_t = \frac{\sum_{i=1}^N (|T_{po,i} - T_{pc,i}| - |T_{po,i} - T_{pa,i}|)}{\sum_{i=1}^N |T_{po,i} - T_{pc,i}|} 100 \quad (A6)$$

[65] Modified correlation coefficient ( $r_{mod}$ : streamflow continuous measure). From *McCuen and Snyder* [1975], this eliminates the regular correlation coefficient's tendency to be overly influenced by outliers and to be insensitive to differences in the hydrograph sizes:

$$r_{mod} = \frac{1}{N} \sum_{i=1}^N \left( r_i \frac{\min \{ \sigma_{sim,i}, \sigma_{obs,i} \}}{\max \{ \sigma_{sim,i}, \sigma_{obs,i} \}} \right) \quad (A7)$$

where  $\sigma_{sim,i}$  and  $\sigma_{obs,i}$  are standard deviations of simulation and observation series, respectively, for the  $i$ th WY,  $r_i$  is corresponding regular correlation coefficient.

[66] Improvement in modified correlation coefficient ( $I_{r_{mod}}$ : streamflow continuous measure)

$$I_{r_{mod}} = \frac{1}{N} \sum_{i=1}^N (r_{mod,a,i} - r_{mod,c,i}) \quad (A8)$$

where  $r_{mod,c,i}$  and  $r_{mod,a,i}$  are the control and assimilation run  $r_{mod}$ , respectively, for the  $i$ th WY.

[67] Times where assimilation better than control ( $B_t$ , %: streamflow continuous measure)

$$B_t = \frac{1}{N} \sum_{i=1}^N \left( \frac{N_{B,i}}{N_i} \right) 100 \quad (\text{A9})$$

where  $N_{B,i}$  is the number of time steps that assimilation residual ( $|Q_{o,ji} - Q_{a,ji}|$ ) < control residual ( $|Q_{o,ji} - Q_{c,ji}|$ ) for the  $i$ th WY,  $N_i$  is corresponding number of time steps,  $Q_{o,ji}$ ,  $Q_{c,ji}$ , and  $Q_{a,ji}$  are the observed, control and assimilation run streamflows, respectively, at the  $j$ th time step.

[68] Streamflow residual improvement during times with better assimilation ( $RI_Q$ , %: streamflow continuous measure)

$$I_R = \frac{1}{N} \sum_{i=1}^N \left[ 100 \left( 1 - \frac{1}{N_{B,i}} \sum_{j=1}^{N_{B,i}} \frac{|Q_{o,ji} - Q_{a,ji}|}{|Q_{o,ji} - Q_{c,ji}|} \right) \right] \quad (\text{A10})$$

where  $Q_{o,ji}$ ,  $Q_{c,ji}$  and  $Q_{a,ji}$  are the observed, control and assimilation run streamflows, respectively, at the  $j$ th time step of the  $i$ th WY.

[69] SWE bias improvement ( $I_W$ , %: SWE continuous measure):

$$I_W = \frac{\sum_{i=1}^N (|W_{om,i} - W_{cm,i}| - |W_{om,i} - W_{am,i}|)}{NW_{om,avg}} 100 \quad (\text{A11})$$

where  $W_{om,i}$ ,  $W_{cm,i}$  and  $W_{am,i}$  are the mean SWEs of reference (basin SNODAS), control run and assimilation run, respectively, for the  $i$ th WY,  $W_{om,avg}$  is average reference mean SWE (basin SNODAS) for  $N$  WYs.

[70] SWE bias residual improvement ( $RI_W$ , %: SWE continuous measure):

$$RI_W = \frac{\sum_{i=1}^N (|W_{om,i} - W_{cm,i}| - |W_{om,i} - W_{am,i}|)}{\sum_{i=1}^N |W_{om,i} - W_{cm,i}|} 100 \quad (\text{A12})$$

[71] SWE centroid date improvement ( $I_C$ , Days: SWE continuous measure):

$$I_C = \frac{\sum_{i=1}^N (|SCD_{o,i} - SCD_{c,i}| - |SCD_{o,i} - SCD_{a,i}|)}{N} \quad (\text{A13})$$

where  $SCD_{o,i}$ ,  $SCD_{c,i}$  and  $SCD_{a,i}$  are the SWE centroid date (days) of observations, control run and assimilation run, respectively, for the  $i$ th WY,

$$[72] \text{ SCD for the } i\text{th WY is } \frac{\sum_{j=1}^{N_i} (j_i * W_{j,i})}{24 * \sum_{j=1}^{N_i} (W_{j,i})},$$

[73]  $j_i$  is the  $j$ th hour, and  $W_{j,i}$  is the SWE at  $j_i$ .

[74] SWE centroid date residual improvement ( $RI_C$ , %: SWE continuous measure):

$$RI_C = \frac{\sum_{i=1}^N (|SCD_{o,i} - SCD_{c,i}| - |SCD_{o,i} - SCD_{a,i}|)}{\sum_{i=1}^N |SCD_{o,i} - SCD_{c,i}|} 100 \quad (\text{A14})$$

[75] **Acknowledgments.** We gratefully acknowledge the support from the NASA Applied Sciences Program Decisions-CAN proposal NN-H-04-Z-YO-010-C (PI: Restrepo). We also acknowledge helpful science and project scheduling discussions with Scott Rheingrover, provision of the correct aesc19\_rms code by Eric Anderson (NOAA, retired), data and basin comparison correspondence with Robert Rice (UC Merced), MODIS data and assimilation communications with Kristi Arsenault (GMU/CREW) and Dorothy Hall and James Foster (NASA/GSFC), and in situ snow data initially provided by NOHRSC and the DMIP2 project. We greatly appreciate the useful review comments and suggestions provided by Editor John Selker, Associate Editor Martyn Clark, two anonymous reviewers and Kristie Franz.

## References

- Anderson, E. A. (1973), National Weather Service river forecast system—Snow accumulation and ablation model, in *NOAA Tech. Memo. NWS HYDRO-17*, 217 pp., U.S. Dep. of Commer., Silver Spring, Md.
- Anderson, E. A. (2002), Calibration of conceptual hydrologic models for use in river forecasting, NOAA's NWS Hydrologic Science and Modeling Branch manual, (Available from <http://www.weather.gov/oh/hrl/hsmh/hydrology/calibration/index.html>), NOAA, Silver Spring, MD.
- Anderson, E. A. (2006), Snow accumulation and ablation model—SNOW-17, NOAA's National Weather Service Hydrology Laboratory NWSRFS user manual, 61 pp., (Available from [http://www.nws.noaa.gov/oh/hrl/nwsrfs/users\\_manual/part2/\\_pdf/22snow17.pdf](http://www.nws.noaa.gov/oh/hrl/nwsrfs/users_manual/part2/_pdf/22snow17.pdf)), NOAA, Silver Spring, MD.
- Andreadis, K. M., and D. P. Lettenmaier (2006), Assimilating remotely sensed snow observations into a macroscale hydrology model, *Adv. Water Resour.*, 29(6), 872–886.
- Armstrong, R. L., and M. J. Brodzik (2001), Recent Northern Hemisphere snow extent: A comparison of data derived from visible and microwave satellite sensors, *Geophys. Res. Lett.*, 28, 3673–3676.
- Arsenault, K. R. (2011), Impact of model and observation Error on assimilating snow cover fraction observations, Ph.D. dissertation, 312 pp., George Mason Univ., Fairfax, Va.
- Barnett, T. P., J. C. Adam, and D. P. Lettenmaier (2005), Potential impacts of a warming climate on water availability in snow-dominated regions, *Nature*, 438, 303–309, doi:10.1038/nature04141.
- Blöschl, G. (1991), The influence of uncertainty in air temperature and albedo on snowmelt, *Nord. Hydrol.*, 22, 95–108.
- Burnash, R. J. C. (1995), The NWS river forecast system—Catchment modeling, in *Computer Models of Watershed Hydrology*, edited by V. P. Singh, pp. 311–366, Water Resour. Publ., Littleton, Colo.
- Carroll, T., D. Cline, G. Fall, A. Nilsson, L. Li, and A. Rost (2001), NOHRSC operations and the simulation of snow cover properties for the conterminous U.S., paper presented at 69th Annual Meeting of the Western Snow Conference, Sun Valley, Idaho, 16–19 Apr.
- Chen, F., K. Mitchell, J. Schaake, Y. Xue, H.-L. Pan, V. Koren, Q. Y. Duan, M. Ek, and A. Betts (1996), Modeling of land surface evaporation by four schemes and comparison with FIFE observations, *J. Geophys. Res.*, 101(D3), 7251–7268, doi:10.1029/95JD02165.
- Clark, M. P., A. G. Slater, A. P. Barrett, L. E. Hay, G. J. McCabe, B. Rajagopalan, and G. H. Leavesley (2006), Assimilation of snow covered area information into hydrologic and land-surface models, *Adv. Water Resour.*, 29(8), 1209–1221, doi:10.1016/j.advwatres.2005.10.001.
- Clark, M. P., J. Hendrikx, A. G. Slater, D. Kavetski, B. Anderson, N. J. Cullen, T. Kerr, E. O. Hreinsson, and R. A. Woods (2011), Representing spatial variability of snow water equivalent in hydrologic and land-surface models: A review, *Water Resour. Res.*, 47, W07539, doi:10.1029/2011WR010745.
- Clifford, D. (2010), Global estimates of snow water equivalent from passive microwave instruments: History, challenges and future developments, *Int. J. Remote Sensing*, 31(14), 3707–3726, doi:10.1080/01431161.2010.483482.

- Cline, D., S. Yueh, S. Nghiem, and K. McDonald (2004), Ku-band radar response to terrestrial snow properties, *EOS Trans. AGU*, 85(47), Fall Meet. Suppl., Abstract H23D-1149.
- Deems, J. S., S. R. Fassnacht, and K. J. Elder (2008), Interannual consistency in fractal snow depth patterns at two Colorado mountain sites, *J. Hydrometeorol.*, 9, 977–988, doi:10.1175/2008JHM901.1.
- De Lannoy, G. J. M., R. H. Reichle, K. R. Arsenault, P. R. Houser, S. Kumar, N. E. C. Verhoest, and V. R. N. Pauwels (2012), Multiscale assimilation of Advanced Microwave Scanning Radiometer–EOS snow water equivalent and Moderate Resolution Imaging Spectroradiometer snow cover fraction observations in northern Colorado, *Water Resour. Res.*, 48, W01522, doi:10.1029/2011WR010588.
- Dettinger, M. D., D. R. Cayan, M. K. Meyer, and A. E. Jeton (2004), Simulated hydrologic responses to climate variations and change in the Merced, Carson, and American River basins, Sierra Nevada, California, 1900–2099, *Clim. Change*, 62, 283–317.
- Dozier, J., T. H. Painter, K. Rittger, and J. E. Frew (2008), Time–space continuity of daily maps of fractional snow cover and albedo from MODIS, *Adv. Water Resour.*, 31, 1515–1526.
- Dressler, K. A., G. H. Leavesley, R. C. Bales, and S. R. Fassnacht (2006), Evaluation of gridded snow water equivalent and satellite snow cover products for mountain basins in a hydrologic model, *Hydrol. Processes*, 20, 673–688.
- Ek, M. B., K. E. Mitchell, Y. Lin, E. Rogers, P. Grunmann, V. Koren, G. Gayno, and J. D. Tarpley (2003), Implementation of Noah land surface model advances in the National Centers for Environmental Prediction operational mesoscale Eta model, *J. Geophys. Res.*, 108, 8851, doi:10.1029/2002JD003296.
- Essery, R., N. Rutter, J. Pomeroy, R. Baxter, M. Stähli, D. Gustafsson, A. Barr, P. Bartlett, and K. Elder (2009), SNOWMIP2: An evaluation of forest snow process simulations, *Bull. Am. Meteorol. Soc.*, 90(8), 1120–1135, doi:10.1175/2009BAMS2629.1.
- Finger, D., F. Pellicciotti, M. Konz, S. Rinkus, and P. Burlando (2011), The value of glacier mass balance, satellite snow cover images, and hourly discharge for improving the performance of a physically based distributed hydrological model, *Water Resour. Res.*, 47, W07519, doi:10.1029/2010WR009824.
- Foster, J. L., A. T. C. Chang, D. K. Hall, and A. Rango (1991), Derivation of snow water equivalent in boreal forests using microwave radiometry, *Arctic*, 44, 147–152.
- Greene, D. R., and M. D. Hudlow (1982), Hydrometeorologic grid mapping procedures, paper presented at AWRA International Symposium on Hydrometeorology, Am. Water Resource. Assoc., Denver, Colo.
- Grünwald, T., M. Schirmer, R. Mott, and M. Lehning (2010), Spatial and temporal variability of snow depth and ablation rates in a small mountain catchment, *Cryosphere*, 4, 215–225, doi:10.5194/tc-4-215-2010.
- Hall, D. K., J. L. Foster, D. L. Verbyla, A. G. Klein, and C. S. Benson (1998), Assessment of snow-cover mapping accuracy in a variety of vegetation-cover densities in Central Alaska, *Remote Sens. Environ.*, 66, 129–137.
- Hall, D. K., J. L. Foster, V. V. Salomonson, A. G. Klein, and J. Y. L. Chien (2001), Development of a technique to assess snow-cover mapping errors from space, *IEEE Trans. Geosci. Remote Sensing*, 39(2), 432–438.
- Hall, D. K., G. A. Riggs, J. L. Foster, and S. V. Kumar (2010), Development and evaluation of a cloud-gap-filled MODIS daily snow-cover product, *Remote Sens. Environ.*, 114, 496–503.
- Hardy, J. P., R. E. Davis, R. Jordan, X. Li, C. Woodcock, W. Ni, and J. C. McKenzie (1997), Snow ablation modeling at the stand scale in a boreal jack pine forest, *J. Geophys. Res.*, 102(D24), 29,397–29,405, doi:10.1029/96JD03096.
- Homan, J. W., C. H. Luce, J. P. McNamara, and N. F. Glenn (2011), Improvement of distributed snowmelt energy balance modeling with MODIS-based NDSI-derived fractional snow-covered area data, *Hydrol. Processes*, 25, 650–660, doi:10.1002/hyp.7857.
- Huttunen, M., I. Huttunen, and B. Vehviläinen (2005), Methods and results using EO data in the SYKE-WSFS hydrological model in boreal drainage basin, *Deliverable 19, D4-WP5, EnviSnow EVGI-CT-2001-00052*, Finnish Environ. Inst. (SYKE), Helsinki, Finland. [Available at <http://www.ymparisto.fi/download.asp?contentid=29987&lan=sv>.]
- Jeton, A. E., M. D. Dettinger, and J. L. Smith (1996), Potential effects of climate change on streamflow, Eastern and Western slopes of the Sierra Nevada, California and Nevada, *U.S. Geol. Surv. Water Resour. Invest. Rep.*, 95-4260, 44 pp.
- Johansson, B., J. Andreasson, and J. Jansson (2003), Satellite data on snow cover in the HBV model. Method development and evaluation, *Rep. 90*, SMHI, Norrköping, Sweden.
- Kolberg, S., and L. Gottschalk (2006), Updating of snow depletion curve with remote sensing data, *Hydrol. Processes*, 20, 2363–2380.
- Kolberg, S., and L. Gottschalk (2010), Interannual stability of grid cell snow depletion curves as estimated from MODIS images, *Water Resour. Res.*, 46, W11555, doi:10.1029/2008WR007617.
- Kolberg, S., H. Rue, and L. Gottschalk (2006), A Bayesian spatial assimilation scheme for snow coverage observations in a gridded snow model, *Hydrol. Earth Syst. Sci.*, 10, 369–381, doi:10.5194/hess-10-369-2006.
- König, M., and M. Sturm (1998), Mapping snow distribution in the Alaskan Arctic using aerial photography and topographic relationships, *Water Resour. Res.*, 34, 3471–3483, doi:10.1029/98WR02514.
- Koren, V. I., M. Smith, D. Wang, and Z. Zhang (2000), Use of soil property data in the derivation of conceptual rainfall-runoff model parameters, in *Proceedings of the 15th Conference on Hydrology*, pp. 103–106, Am. Meteorol. Soc., Long Beach, Calif.
- Koren, V., S. Reed, M. Smith, Z. Zhang, and D.-J. Seo (2004), Hydrology laboratory research modeling system (HL-RMS) of the US national weather service, *J. Hydrol.*, 291, 297–318.
- Koren, V., M. Smith, Z. Cui, and B. Cosgrove (2007), Physically-based modifications to the sacramento soil moisture accounting model: Modeling the effects of frozen ground on the runoff generation process, *NOAA Tech. Rep. 52*, 43 pp., U.S. Dep. of Commer., Silver Spring, Md.
- Kumar, S. V., et al. (2006), Land information system—An interoperable framework for high resolution land surface modeling, *Environ. Modell. Software*, 21, 1402–1415.
- Kuzmin, V., D.-J. Seo, and V. Koren (2008), Fast and efficient optimization of hydrologic model parameters using a priori estimates and stepwise line search, *J. Hydrol.*, 353(1–2), 109–128, doi:10.1016/j.jhydrol.2008.02.001.
- Li, X., and M. W. Williams (2008), Snowmelt runoff modeling in an arid mountain watershed, Tarim Basin, China, *Hydrol. Processes*, 22, 3931–3940.
- Liston, G. E. (1999), Interrelationships among snow distribution, snowmelt, and snow cover depletion: Implications for atmospheric, hydrologic, and ecologic modeling, *J. Appl. Meteorol.*, 38, 1474–1487.
- Liston, G. E. (2004), Representing subgrid snow cover heterogeneities in regional and global models, *J. Clim.*, 17, 1381–1397.
- Liston, G. E., R. A. Pielke Sr., and E. M. Greene (1999), Improving first-order snow-related deficiencies in a regional climate model, *J. Geophys. Res.*, 104, 19,559–19,567.
- Liu, J., R. A. Melloh, C. E. Woodcock, R. E. Davis, T. H. Painter, and C. McKenzie (2008), Modeling the view angle dependence of gap fractions in forest canopies: Implications for mapping fractional snow cover using optical remote sensing, *J. Hydrometeorol.*, 9(5), 1005–1019, doi:10.1175/2008JHM866.1.
- Luce, C. H., and D. G. Tarboton (2004), The application of depletion curves for parameterization of subgrid variability of snow, *Hydrol. Processes*, 18, 1409–1422, doi:10.1002/hyp.1420.
- Luce, C. H., D. G. Tarboton, and K. R. Cooley (1998), The influence of the spatial distribution of snow on basin-averaged snowmelt, *Hydrol. Processes*, 12, 1671–1683, doi:10.1002/(SICI)1099-1085(199808/09)12:10<1671::AID-HYP688>3.0.CO;2-N.
- Luce, C. H., D. G. Tarboton, and K. R. Cooley (1999), Sub-grid parameterization of snow distribution for an energy and mass balance snow model, *Hydrol. Processes*, 13, 1921–1933, doi:10.1002/(SICI)1099-1085(199909)13:12/13<1921::AID-HYP867>3.0.CO;2-S.
- Lundquist, J. D., P. J. Neiman, B. Martner, A. B. White, D. J. Gottas, and F. M. Ralph (2008), Rain versus snow in the Sierra Nevada, California: Comparing Doppler profiling radar and surface observations of melting level, *J. Hydrometeorol.*, 9, 194–211.
- McCuen, R. H., and W. M. Snyder (1975), A proposed index for comparing hydrographs, *Water Resour. Res.*, 11(6), 1021–1024.
- McGuire, M., A. W. Wood, A. F. Hamlet, and D. P. Lettenmaier (2006), Use of satellite data for streamflow and reservoir storage forecasts in the Snake River Basin, *J. Water Resour. Plann. Manage.*, 132(2), 97–110, doi:10.1061/(ASCE)0733-9496(2006)132:2(97).
- Mizukami, N., and V. Koren (2008), Methodology and evaluation of melt factor parameterization for distributed SNOW-17, paper presented at AGU Fall Meeting, December 2008, San Francisco, Calif.
- Molotch, N. P., and S. A. Margulis (2008), Estimating the distribution of snow water equivalent using remotely sensed snow cover data and a spatially distributed snowmelt model: A multi-resolution, multi-sensor comparison, *Adv. Water Resour.*, 31(11), 1503–1514.
- Musselman, K. N., N. P. Molotch, and P. D. Brooks (2008), Effects of vegetation on snow accumulation and ablation in a mid-latitude sub-alpine forest, *Hydrol. Processes*, 22, 2767–2776.

- Nagler, T., H. Rott, P. Malcher and F. Muller (2008), Assimilation of meteorological and remote sensing data for snowmelt runoff forecasting, *Remote Sens. Environ.*, **112**, 1408–1420.
- National Operational Hydrologic Remote Sensing Center (NOHRSC) (2004), *Snow Data Assimilation System (SNODAS) Data Products at NSIDC*, digital media, Natl. Snow and Ice Data Center, Boulder, Colo.
- Nijssen, B., et al. (2003), Simulation of high latitude hydrological processes in the Torne-Kalix basin: PILPS Phase 2(e) 2: Comparison of model results with observations, *Global Planet. Change*, **38**, 31–53.
- Painter, T. H., K. Rittger, C. McKenzie, P. Slaughter, R. E. Davis, and J. Dozier (2009), Retrieval of subpixel snow covered area, grain size, and albedo from MODIS, *Remote Sens. Environ.*, **113**, 868–879.
- Parajka, J., and G. Blöschl (2008), The value of MODIS snow cover data in validating and calibrating conceptual hydrologic models, *J. Hydrol.*, **358**, 240–258.
- Peters-Lidard, C. D., et al. (2007), High-performance Earth system modeling with NASA/GSFC's land information system, *Innovations Syst. Software Eng.*, **3**(3), 157–165.
- Pinty, B., et al. (2004), Radiation Transfer Model Intercomparison (RAMI) exercise: Results from the second phase, *J. Geophys. Res.*, **109**, D06210, doi:10.1029/2003JD004252.
- Pomeroy, J. W., and K. Dion (1996), Winter radiation extinction and reflection in a boreal pine canopy: Measurements and modelling, *Hydrol. Processes*, **10**, 1591–1608.
- Pomeroy, J. W., and R. G. Granger (1997), Sustainability of the western Canadian boreal forest under changing hydrological conditions. 1. Snow accumulation and ablation, in *Symposium 1 - Sustainability of Water Resources Under Increasing Uncertainty*, IAHS Publ. 240, pp. 237–242, Int. Assoc. Hydrol. Soc. Press, Wallingford, U.K.
- Pulliainen, J., J. Koskinen, and M. Hallikainen (2001), Compensation of forest canopy effects in the estimation of snow covered area from SAR data, *IEEE Geosci. Remote Sens. Symp.*, **2**, 813–815, doi:10.1109/IGARSS.2001.976645.
- Reed, S. M. (2003), Deriving flow directions for coarse-resolution (1–4 km) gridded hydrologic modeling, *Water Resour. Res.*, **39**(9), 1238, doi:10.1029/2003WR001989.
- Rice, R., R. Bales, P. Kirchener, K. Rittger, T. H. Painter, and J. Dozier (2010), Canopy-adjustment of the MODIS fractional snow covered area in forest catchments in the Sierra Nevada, paper presented at Remote Sensing and Hydrology 2010 Symposium, Jackson Hole, Wyo.
- Riggs, G. A., D. K. Hall, and V. V. Salomonson, (2006), *MODIS Snow Products User Guide to Collection 5*, 80 pp., NASA, Washington, DC. [Available at [http://modis-snow-ice.gsfc.nasa.gov/uploads/sug\\_c5.pdf](http://modis-snow-ice.gsfc.nasa.gov/uploads/sug_c5.pdf).]
- Robin, J., R. Dubayah, E. Sparrow, and E. Levine (2007), Monitoring start of season in Alaska with GLOBE, AVHRR, and MODIS data, *J. Geophys. Res.*, **113**, G01017, doi:10.1029/2007JG000407.
- Rodell, M., and P. R. Houser (2004), Updating a land surface model with MODIS-derived snow cover, *J. Hydrometeorol.*, **5**, 1064–1075.
- Roy, A., A. Royer, and R. Turcotte (2010), Improvement of springtime streamflow simulations in a boreal environment by incorporating snow-covered area derived from remote sensing data, *J. Hydrol.*, **390**, 35–44.
- Rutter, N., et al. (2009), Evaluation of forest snow processes models (SnowMIP2), *J. Geophys. Res.*, **114**, D06111, doi:10.1029/2008JD011063.
- Salomonson, V. V., and I. Appel (2004), Estimating fractional snow cover from MODIS using the normalized difference snow index, *Remote Sens. Environ.*, **89**, 351–360.
- Salomonson, V. V., and I. Appel (2006), Development of the Aqua MODIS NDSI fractional snow cover algorithm and validation results, *IEEE Trans. Geosci. Remote Sens.*, **44**(7), 1747–1756.
- Schaeffli, B., and H. V. Gupta (2007), Do Nash values have value?, *Hydrol. Processes*, **21**, 2075–2080, doi:10.1002/hyp.6825.
- Schmid, W., and R. T. Hanson (2009), Appendix 1, Supplemental Information—Modifications to Modflow-2000 Packages and Processes, in *Groundwater Availability of the Central Valley Aquifer, California, U.S. Geol. Surv. Prof. Pap. 1776*, edited by C. C. Faunt, pp. 213–225, U.S. Geol. Surv., Reston, Virginia. [Available at [http://pubs.usgs.gov/pp/1766/PP\\_1766.pdf](http://pubs.usgs.gov/pp/1766/PP_1766.pdf).]
- Serreze, M. C., M. P. Clark, and A. Frei (2001), Characteristics of large snowfall events in the montane western United States as examined using snowpack telemetry (SNOTEL) data, *Water Resour. Res.*, **37**(3), 675–688, doi:10.1029/2000WR900307.
- Sicart, J.-E., J. W. Pomeroy, R. L. H. Essery, J. Hardy, T. Link, and D. Marks (2004), A sensitivity study of daytime net radiation during snowmelt to forest canopy and atmospheric conditions, *J. Hydrometeorol.*, **5**, 774–784.
- Simic, A., R. Fernandes, R. Brown, P. Romanov, and W. Park (2004), Validation of VEGETATION, MODIS, and GOES+ SSM/I snow-cover products over Canada based on surface snow depth observations, *Hydrol. Processes*, **18**, 1089–1104.
- Simpson, J. J., M. D. Dettinger, F. Gehrke, T. J. McIntire, and G. L. Huffurd (2004), Hydrologic scales, cloud variability, remote sensing, and models: Implications for forecasting snowmelt and streamflow, *Weather Forecast.*, **19**, 251–276.
- Slater, A. G., and M. P. Clark (2006), Snow data assimilation via an ensemble Kalman filter, *J. Hydrometeorol.*, **7**(3), 478–493.
- Smith, M. B., D. P. Laurine, V. I. Koren, S. M. Reed, and Z. Zhang (2003), Hydrologic model calibration in the National Weather Service, in *Calibration of Watershed Models*, *Water Sci. Appl.*, vol. 6, edited by Q. Duan et al., pp. 133–152, AGU, Washington, D.C.
- Smith, M. B., D.-J. Seo, V. I. Koren, S. M. Reed, Z. Zhang, Q. Duan, F. Moreda, and S. Cong (2004), The distributed model intercomparison project (DMIP): Motivation and experiment design, *J. Hydrol.*, **298**, 4–26.
- Smith, M., F. Ding, Z. Cui, V. Koren, N. Mizukami, Z. Zhang, B. Cosgrove, D. Kitzmiller, and J. Schaake (2010a), Development of gridded QPE datasets for mountainous area distributed hydrologic modeling, paper presented at ASCE EWRI conference, Am. Soc. of Civil Eng., Providence, Rhode Island, 16–20, May.
- Smith, M., V. Koren, Z. Zhang, N. Mizukami, Z. Cui, B. Cosgrove, F. Ding, Y. Zhang, and D. Kitzmiller (2010b), Overall DMIP 2 western basin results, NOAA interim report, U. S. Dep. of Commer., Silver Spring, Md.
- Su, H., Z.-L. Yang, G.-Y. Niu, and R. E. Dickinson (2008), Enhancing the estimation of continental-scale snow water equivalent by assimilating MODIS snow cover with the ensemble Kalman filter, *J. Geophys. Res.*, **113**, D08120, doi:10.1029/2007JD009232.
- Tang, Q., and D. P. Lettenmaier (2010), Use of satellite snow-cover data for streamflow prediction in the Feather River Basin, California, *Int. J. Remote Sensing*, **31**(14), 3745–3762.
- Thirel, G., P. Salamon, P. Burek, and M. Kalas (2011), Assimilation of MODIS snow cover area data in a distributed hydrological model, *Hydrol. Earth Syst. Sci. Discuss.*, **8**, 1329–1364, doi:10.5194/hessd-8-1329-2011.
- Udnes, H.-C., E. Alfnes, and L. M. Andreassen (2007), Improving runoff modeling using satellite-derived snow cover area?, *Nordic Hydrol.*, **38**(1), 21–32, doi:10.2166/nh.2007.032.
- Varhola, A., N. C. Coops, M. Weiler, and R. D. Moore (2010), Forest canopy effects on snow accumulation and ablation: An integrative review of empirical results, *J. Hydrol.*, **392**, 219–233, doi:10.1016/j.jhydrol.2010.08.009.
- Vikhamar, D., and R. Solberg (2002), Subpixel mapping of snow cover in forests by optical remote sensing, *Remote Sens. Environ.*, **84**, 69–82.
- Zaitchik, B. F., and M. Rodell (2009), Forward-looking assimilation of MODIS-derived snow-covered area into a land surface model, *J. Hydrometeorol.*, **10**(1), 130–148.
- Zhang, Y., Z. Zhang, S. Reed, and V. Koren (2011), An enhanced and automated approach for deriving a priori SAC-SMA parameters from the Soil Survey Geographic Database, *Comput. Geosci.*, **37**(2), 219–231, doi:10.1016/j.cageo.2010.05.016.